Electronic Delivery Cover Sheet


PERGAMON

Journal of the Mechanics and Physics of Solids
51 (2003) 425–460

JOURNAL OF THE
MECHANICS AND
PHYSICS OF SOLIDS

www.elsevier.com/locate/jmps

Dynamic crack growth along a polymer composite–Homalite interface

D. Coker[a], A.J. Rosakis[b], A. Needleman[a,*]

[a] *Division of Engineering, Brown University, Box D, Providence, RI 02912-9104, USA*
[b] *Division of Engineering and Applied Science, California Institute of Technology, Pasadena, CA 91125, USA*

Received 11 March 2002; received in revised form 24 July 2002; accepted 30 July 2002

Abstract

Dynamic crack growth along the interface of a fiber-reinforced polymer composite–Homalite bimaterial subjected to impact shear loading is investigated experimentally and numerically. In the experiments, the polymer composite–Homalite specimens are impacted with a projectile causing shear dominated interfacial cracks to initiate and subsequently grow along the interface at speeds faster than the shear wave speed of Homalite. Crack growth is observed using dynamic photoelasticity in conjunction with high-speed photography. The calculations are carried out for a plane stress model of the experimental configuration and are based on a cohesive surface formulation that allows crack growth, when it occurs, to emerge as a natural outcome of the deformation history. The effect of impact velocity and loading rate is explored numerically. The experiments and calculations are consistent in identifying discrete crack speed regimes within which crack growth at sustained crack speeds is possible. We present the first conclusive experimental evidence of interfacial crack speeds faster than any characteristic elastic wave speed of the more compliant material. The occurrence of this crack speed was predicted numerically and the calculations were used to design the experiments. In addition, the first experimental observation of a mother–daughter crack mechanism allowing a subsonic crack to evolve into an intersonic crack is documented. The calculations exhibit all the crack growth regimes seen in the experiments and, in addition, predict a regime with a pulse-like traction distribution along the bond line.

Keywords: Dynamic fracture; Intersonic crack speed; Interface fracture; Bimaterials

* Corresponding author. Tel.: +1-401-863-2863; fax: +1-401-863-1157.
E-mail address: needle@engin.brown.edu (A. Needleman).

0022-5096/03/$ - see front matter
PII: S0022-5096(02)00082-0

1. Introduction

Composite–metal and composite–polymer interfaces are found in many engineering applications such as the new generation of marine structures, lightweight missiles, turbine blades, etc. The adhesive bonding of anisotropic composites to other isotropic constituents is generally favored over bolting since it increases the reliability of the structure by avoiding puncturing. Under dynamic loading conditions, failure usually takes place at the bonded interfaces, with failure along such interfaces often involving cracks running at speeds comparable to the wave speeds of the constituent materials. In this paper, we carry out an experimental and numerical investigation of intersonic and supersonic interfacial crack growth in a fiber-reinforced polymer composite–Homalite bimaterial. We use the term intersonic crack speed to refer to a crack speed between the shear and longitudinal elastic wave speeds of the more compliant material and the term supersonic crack speed to refer to a crack speed greater than the longitudinal wave speed of the more compliant material.

A fundamental question in dynamic fracture mechanics concerns the limit on attainable crack speeds. For remotely loaded cracks in homogeneous isotropic elastic solids, the energy flux into the crack tip vanishes as the crack speed increases to the Rayleigh wave speed of the material (Broberg, 1960; Freund, 1998). Experimentally, under tensile (mode I) loading conditions crack speeds rarely attain half the Rayleigh wave speed in monolithic materials, with crack branching and attempted crack branching playing a major role in limiting the crack speed, see e.g. Ravi-Chandar and Knauss (1984), Xu and Needleman (1994), Sharon et al. (1996), Sharon and Fineberg (1999). Under mixed-mode or shear (mode II) loading conditions, cracks tend to deviate from a straight path unless such cracks are trapped by a weak prescribed path or by an interface. Theoretically, mode II cracks confined to propagate along a prescribed straight line path, can undergo sustained propagation at speeds between the shear wave speed and the longitudinal wave of the material (Freund, 1979; Broberg, 1989). Direct experimental evidence for crack growth with a crack speed above the shear wave speed in a homogeneous elastic solid subject to remote loading was obtained by Rosakis et al. (1999) who introduced a weak plane in a Homalite specimen subject to mode II loading.

Within the framework of classical fracture mechanics, mode II crack speeds between the Rayleigh wave speed and the shear wave speed are forbidden. One way a mode II crack propagating along a prescribed path (weak plane or interface) can attain higher speeds is for it to begin propagating intersonically as soon as it nucleates. Another mechanism involves the nucleation of a daughter crack in front of the subsonically growing main crack and the subsequent coalescence of the mother and daughter cracks that together continue propagating at intersonic speeds. Both these mechanisms have been seen in numerical calculations (Burridge, 1973; Andrews, 1976; Needleman, 1999; Abraham and Gao, 2000; Geubelle and Kubair, 2001; Abraham, 2001) but, until now, there has not been any direct experimental observation of the mother–daughter crack mechanism.

For an anisotropic composite, Coker and Rosakis (2001) experimentally observed that mode II cracks constrained to move along the major direction of anisotropy (the crack path along the fibers) spontaneously become intersonic, reaching the longitudinal

wave speed of the transversely isotropic composite and then settling down to a speed near the speed that analytical solutions (Piva and Hasan, 1996; Huang et al., 1999; Gao et al., 1999) show is the unique one corresponding to a finite energy release rate. Motivated by these experiments, computations using a cohesive surface formulation have shown that shear cracks in orthotropic materials can indeed accelerate up to the longitudinal wave speed and eventually settle down to a steady state speed that depends on the cohesive strength and on the loading pulse duration (Yu et al., 2002; Hwang and Geubelle, 2000; Dwivedi and Espinosa, 2002). In Yu et al. (2002) and Hwang and Geubelle (2000), the composite materials were treated as homogeneous orthotropic solids and their success in describing the experimental observations demonstrates the appropriateness of homogenization of constitutive properties provided that fracture toughness inhomogeneity is properly accounted for by allowing for the existence of a preferable crack path along the fibers.

Bimaterial interfaces, in addition to their engineering importance, provide an attractive system for experimental studies of fast crack growth because the interfacial strength can be adjusted to confine the crack to the bond line. For crack growth along a bimaterial interface, any in-plane loading results in mixed mode I (tensile) and mode II (shear) conditions near the crack tip. An overview of dynamic fracture along interfaces is given by Rosakis (2002). Intersonic crack propagation was first observed in polymer–metal bimaterials experimentally by Liu et al. (1993), Lambros and Rosakis (1995), Singh and Shukla (1996), Singh et al. (1997). These experimental results motivated analytical (Liu et al., 1995; Yu and Yang, 1995; Huang et al., 1998, 1999; Brock, 2002) and numerical work (Lo et al., 1994; Xu and Needleman, 1996; Breitenfeld and Geubelle, 1997; Needleman and Rosakis, 1999) that gave rise to predictions largely consistent with the experimental observations. The numerical calculations also showed a strong dependence of the crack speed on the mismatch in elastic properties across the bond line, on the impact velocity and on the bond strength. However, these studies of bimaterial crack propagation have not conclusively resolved the issues of regimes of favorable crack speeds and of limiting crack speeds within a general bimaterial setting.

The polymer composite–Homalite bimaterial in the experiments here has a very high longitudinal wave speed mismatch, but has a small density and shear wave speed mismatch. Furthermore, while previous numerical calculations using a cohesive surface formulation have reproduced key features of fast crack growth seen experimentally, the extent to which this framework can actually *predict* phenomena has not been tested. A special feature of the present study is that the numerical calculations were used to design experiments to identify crack speed regimes attainable under given loading conditions, including a crack speed regime where the longitudinal wave speed of the more compliant material was exceeded.

We begin by describing the experimental techniques. The bimaterial specimens are impacted with a projectile in such a way as to cause mode II dominated interfacial crack growth. A particular issue is designing the bimaterial system and loading configuration so that the crack is constrained to grow along the bond line. Measurements are made using the dynamic photoelasticity method. Next, the calculations are described which were carried out using a cohesive surface decohesion formulation (Needleman, 1987; Xu and Needleman, 1994) where the failure characteristics are embodied in

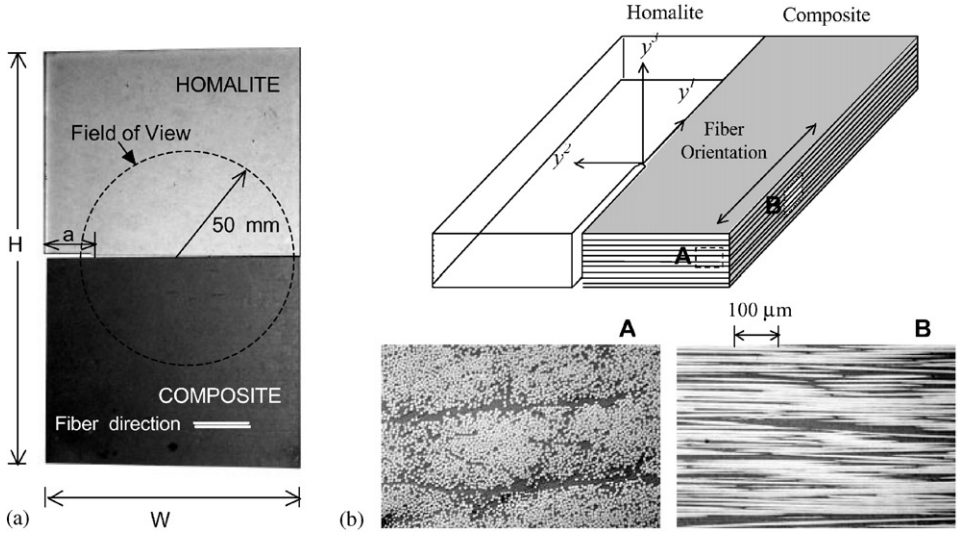

Fig. 1. (a) Photograph of the Homalite and graphite/epoxy composite bimaterial specimen: $H = 200$ mm, $W = 125$ mm, $a = 25$ mm and the thickness is 6.7 mm. (b) Cross-section view of the fiber-reinforced unidirectional graphite/epoxy composite material.

a phenomenological constitutive relation that describes separation along one or more cohesive surfaces. Within this cohesive surface framework, the continuum is characterized by two constitutive relations; one that relates stress and deformation in the bulk material, the other that relates the traction and displacement jump across a cohesive surface. These constitutive relations together with appropriate balance laws and initial and boundary conditions completely specify the initial-boundary problem so that fracture, when it occurs, emerges as a natural outcome of the loading history. The presentation of the results focuses on the crack speed histories and the stress state in the Homalite. Both the experiments and the calculations show that there are distinct regimes of more or less steady crack speed, depending on the loading configuration and loading rate. The near crack tip stress state differs significantly in the various crack speed regimes.

2. Experimental method

2.1. Material and specimen geometry

The bimaterial specimens consist of a unidirectional graphite fiber-reinforced epoxy matrix composite material bonded to Homalite-100, a polyester resin that exhibits stress-induced birefringence, Fig. 1a. The material properties and wave speeds for Homalite-100 are listed in Table 1 (Rosakis et al., 1998). All properties listed are dynamic properties (at a strain rate of the order of 10^3/s) and both plane-strain and plane-stress values for the wave speeds are given.

The composite plates were manufactured by Composite Mirror Applications, AZ, from 48 layers of graphite fiber and epoxy matrix pre-pregs laid up in the thickness

Table 1
Dynamic material properties, wave speeds and static strengths for Homalite-100 and for the graphite fiber-reinforced epoxy composite

	Homalite-100	Composite
Young's modulus (GPa)	$E = 5.2$	$E^{\parallel} = 80.0$ $E^{\perp} = 8.9$
Shear modulus (GPa)	$\mu = 1.9$	$\mu_{12} = 3.6$
Poisson's ratio	$\nu = 0.34$	$\nu_{12} = 0.25$
Mass density (kg/m^3)	$\rho = 1230$	$\rho = 1478$
Shear wave speed (m/s)	$c_s = 1255$	$c_s = 1560$
Longitudinal wave speed (plane-strain) (m/s)	$c_l = 2560$	$c_l^c = c_l^{\parallel} = 7450$ $c_l^{\perp} = 2740$
Longitudinal wave speed (plane-stress) (m/s)	$c_l = 2187$	$c_l^c = c_l^{\parallel} = 7380$ $c_l^{\perp} = 2470$
Rayleigh wave speed (plane-stress) (m/s)	$c_R = 1155$	$c_R = 1548$
Static tensile strength (MPa)	$\sigma_0 = 48$	$\sigma_0 = 36$
Static shear strength (MPa)	$\tau_0 = 42$	$\tau_0 = 27$

direction to form a plate 6.3 mm thick. The fiber diameter is 7.3 μm and the volume fraction of the fibers in the pre-preg is 60–65%. A cross-section view of the composite is shown in Fig. 1b. If y^1 is taken to be in the direction of the fibers, we then assume that the y^2–y^3 plane perpendicular to y^1 is isotropic since the fibers are randomly distributed. This allows us to treat the composite material macroscopically as a transversely isotropic material. Relevant homogenized material properties and wave speeds are presented in Table 1. These values were obtained by Coker and Rosakis (2001) using both static and ultrasonic measurements with pressure and shear transducers operating at a frequency of 5 MHz. Wave speeds both parallel ($c^{\parallel}$) and perpendicular ($c^{\perp}$) to the fibers are shown. Although epoxy is known to be strongly rate dependent, the rate independence of the graphite fiber properties has a dominant effect on the homogenized mechanical properties (Coker and Rosakis, 2001). The bar wave speed in the graphite fiber is 11,230 m/s and the longitudinal wave speed in epoxy is 2500 m/s. Here, the relevant longitudinal wave speed for the composite is that parallel to the fibers, $c^{\parallel}$, and is subsequently denoted by c_l^c. The mismatch in longitudinal wave speed between the composite and Homalite-100 is large, $c_l^c/c_l^H = 3.4$, but the mismatch in shear wave speeds is small, $c_s^c/c_s^H = 1.2$. This is a much larger mismatch in longitudinal wave speed than in the metal and polymer bimaterials used in previous investigations (Rosakis et al., 1998; Singh et al., 1997).

The specimen configuration and dimensions are shown in Fig. 1a, with $W = 127$ mm and $L = 300$ mm. An initial notch, 25 mm long and 2.3 mm wide, was machined along the bond line at one edge of the Homalite-100 half. The composite was oriented such that the fibers were parallel to the bond line. The Homalite part, as machined, was bonded to the composite using two adhesives: Weld-on 10 which is a two-part adhesive consisting of methylmethacrylate monomer base resin and a catalyst containing

methylethylketone, and Super Glue which is a single-component adhesive consisting of ethylcyanoacrylate. The strength of the bond depends on the materials bonded and the curing conditions; Xu and Rosakis (2002) measured values of 25 MPa and greater for aluminum–Homalite bimaterials using these adhesives. Although the strength of the composite–Homalite bond is not known quantitatively, it is sufficiently weak to trap shear dominated cracks along the bond line.

2.2. Experimental setup

The experimental setup used is similar to the one used in previous investigations (for details see Singh and Shukla, 1996; Rosakis et al., 1999). The bimaterial specimen was subjected to impact loading on the edge through either a 25 or a 50 mm diameter steel projectile using a pressurized gas gun with impact velocities of 20–50 m/s. A coherent, monochromatic, plane-polarized laser beam collimated at 100 mm is transmitted through the transparent Homalite half of the specimen. The stress field in the Homalite part is observed using dynamic photoelasticity in conjunction with high-speed photography.

Two sheets of circular polarizers (a $\frac{1}{4}$-wave plate together with a linear polarizer) are placed on both sides of the specimen to form a circular polariscope. This allows us to use photoelasticity to observe the stress-state in a birefringent material such as Homalite. The method of photoelasticity has been extensively described in Dally and Riley (1991) while many applications of dynamic photoelasticity have been discussed by Dally (1978). The generation of the isochromatic fringe pattern is governed by the stress optic law, which provides the relationship between the fringe order at a point and the local in-plane principal stress components as

$$\sigma_1 - \sigma_2 = 2\tau_{\max} = \frac{F_\sigma}{h} N, \tag{1}$$

where F_σ is the material fringe constant associated with the incident light wave length, λ, h is the specimen thickness, and N is the isochromatic fringe order. For Homalite-100, $F_\sigma = 22.6$ kN/m at a wavelength of 514.5 nm, and $h = 6.4$ mm.

The resulting isochromatic fringe pattern was captured in real time on the film track of a rotating-mirror-type high-speed camera (Cordin model 330A) with a lens. The camera is capable of recording 80 frames at framing rates of up to 2×10^6 frames/s (0.5 μs interframe time). In the current experiments, the interframe time was 2.32 μs and the image was recorded on 35 mm black-and-white KODAK TMAX-400 film. The laser used was an argon-ion laser operating at a wavelength of 514.5 nm in a pulsed mode of 8 ns pulse width. The recording process of the event commenced with the impact of the projectile on a strain gage mounted on the point of impact, leading to a sharp voltage jump, thus triggering pulsing of the laser. In some of the experiments, a Cordin 220 high-speed digital camera was used that is capable of framing rates of up to 100 million frames/s and that can record 16 frames in an experiment.

The specimens were impacted with a steel projectile in three different impact configurations as illustrated in Fig. 2. The three configurations involve: (a) impacting the composite on the notch side (case 1), (b) impacting Homalite-100 on the notch side (case 2) and (c) impacting the composite on the side opposite the notch (case 3). All

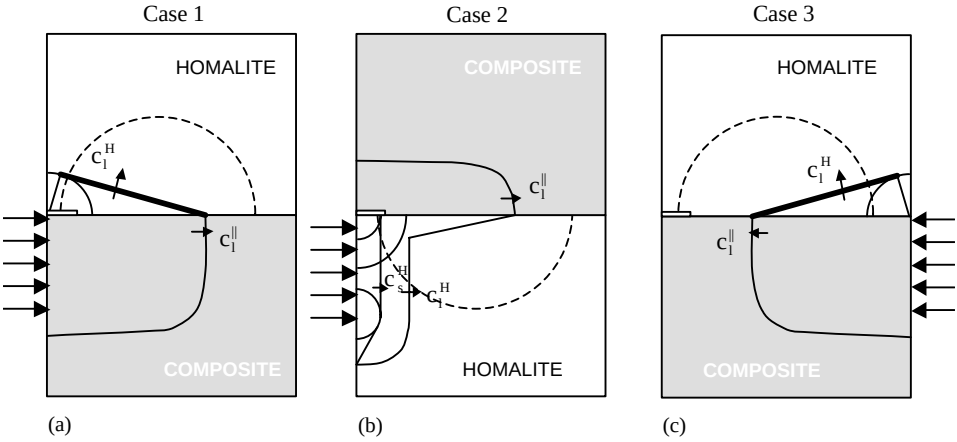

Fig. 2. Specimen geometry and loading methods used to investigate crack speed regimes in the Homalite–composite bimaterial and schematic of the loading waves in the specimen for (a) case 1: impact of the composite half on the notch side, (b) case 2: impact of Homalite half on the notch side, (c) case 3: impact of the composite half opposite to the notch side. The dotted line shows the field of view in the experiments.

three loading configurations result in an interface crack being loaded primarily in shear. The geometry at the point of impact was varied to increase the amount of shearing at the notch tip. In some tests, a steel piece was bonded to the specimen on the impact site to prevent shattering of the Homalite or crushing of the composite, and to induce a more or less planar wave front. When the steel plate is used, the impact edge closest to the bond is 25 mm below the line of the interface, otherwise the impact edge is directly on the bond line.

2.3. Impact wave loading

Fig. 2 shows a schematic of the specimen together with the development of the wave front for the three cases. For case 1, where the composite is impacted on the side with the machined notch, Fig. 2a, a compressive loading wave front travels at $c_1^c = 7380$ m/s in the composite. Energy is transferred across the interface due to the bond between the composite and the Homalite. A head wave appears in the Homalite because the speed of the loading wave in the composite is greater than c_1^H. Under this type of loading the crack has a tendency to grow into the Homalite due to its relatively low toughness. However, if the interfacial bond is weak enough, shear dominated crack growth along the interface is still possible for certain impact velocities. In case 1, the sliding of the composite, relative to the Homalite, is in the direction of crack growth.

For case 2, where the Homalite side is impacted on the notch edge, Fig. 2b, the stress wave front progresses at the longitudinal wave speed of Homalite. When the wave front reaches the bond line, it also spreads in to the composite in which it travels at the longitudinal wave speed of the composite. This wave front then loads the Homalite at the interface far ahead of the initial wave front in Homalite. However, most of the wave energy and the highest particle velocity are in the Homalite, which loads the crack in shear. Under this loading there is a tendency for the crack to grow into the

composite in mode I. However, the high toughness of the composite perpendicular to the fibers traps the crack in the bond line.

In Fig. 2c, case 3, where the composite is loaded along the opposite edge from the notch, the loading wave causes a head wave in the Homalite due to the high longitudinal wave speed in the composite. The main compressive longitudinal stress reaches the notch tip and loads the crack primarily in shear. At a later time, when the compressive loading wave is reflected from the edge as a tensile wave, the horizontal component of the particle velocity in the composite is doubled, enhancing the state of shear around the crack tip. In the experiments with the case 3 configuration, the crack typically initiates under the action of the reflected (tensile) wave and, after the reflected wave reaches the crack tip, the stress normal to the interface is tensile (through the weak Poisson's ratio effect) so that the resulting crack tip loading is one of shear and tension in contrast to shear and compression in cases 1 and 2. The wave reflection does not change the direction of sliding along the bond line. In both cases 2 and 3, the direction of sliding of the Homalite (the more compliant material), relative to the composite, is the same as the direction of crack growth.

3. Computational method

As in Needleman and Rosakis (1999) and Needleman (1999), a finite strain Lagrangian formulation is used, with the initial undeformed configuration taken as reference, with all field quantities considered to be functions of convected coordinates y^i and time t. The principle of virtual work is written as

$$\int_V \mathbf{S} : \delta\mathbf{E}\,\mathrm{d}V - \int_{S_{\mathrm{int}}} \mathbf{T}\cdot\delta\boldsymbol{\Delta}\,\mathrm{d}S = \int_{S_{\mathrm{ext}}} \mathbf{T}\cdot\delta\mathbf{u}\,\mathrm{d}S - \int_V \rho\,\frac{\partial^2\mathbf{u}}{\partial t^2}\cdot\delta\mathbf{u}\,\mathrm{d}V, \tag{2}$$

where $\mathbf{S}$ is the second Piola–Kirchhoff stress tensor, $\mathbf{u}$ is the displacement vector, $\boldsymbol{\Delta}$ is the displacement jump across the cohesive surface, $\mathbf{A}:\mathbf{B}$ denotes $A^{ij}B_{ji}$, and V, S_{ext} and S_{int} are the volume, external surface area and internal cohesive surface area, respectively, of the body in the reference configuration. The density of the material in the reference configuration is ρ, $\mathbf{T}$ is the traction vector and the Lagrangian strain, $\mathbf{E}$, is given by

$$\mathbf{E} = \frac{1}{2}(\mathbf{F}^T\cdot\mathbf{F} - \mathbf{I}), \qquad \mathbf{F} = \mathbf{I} + \frac{\partial\mathbf{u}}{\partial\mathbf{x}} \tag{3}$$

with $\mathbf{I}$ the identity tensor and $\mathbf{x}$ denoting the position vector of a material point in the reference configuration.

In contrast to Needleman and Rosakis (1999) and Needleman (1999), where plane strain conditions were considered, the computations here are reported for a plane stress edge-cracked bimaterial specimen because the plane stress elastic wave speeds were found to give a more accurate representation of the experimental behavior in the context of a two-dimensional idealization. Although only plane stress results are presented, plane strain calculations were also carried out and the results are qualitatively the same and quantitatively the differences are of the order of the elastic wave speed difference. Furthermore, even though a finite strain formulation is used, the strains remain small enough nearly everywhere for the linear elastic idealization to be appropriate.

The specimen has height $L = 300$ mm, width $w = 125$ mm and a crack of length $a_i = 25$ mm. A Cartesian coordinate system is used with all field quantities functions of y^1 and y^2. The origin of the coordinate system is taken to be at the initial crack tip.

At $t = 0$, the body is stress free and at rest. A normal velocity is prescribed either on the edge $y^1 = -a_i$ or on the edge $y^1 = w - a_i$. In both cases, impact occurs in the interval $-b \leqslant y^2 \leqslant 0$, with $b = 50$ mm, and with the shear traction taken to vanish there. The remaining external surfaces of the specimen are traction free. Hence, the boundary conditions are

$$T^1 = 0, \quad T^2 = 0 \quad \text{on } y^2 = 0 \text{ and } y^1 < 0, \tag{4}$$

$$T^1 = 0, \quad T^2 = 0 \quad \text{on } y^2 = \pm L/2, \ y^1 = -a_i, \tag{5}$$

$$T^1 = 0, \quad T^2 = 0 \quad \text{on } y^1 = -a_i \text{ where } y^2 > 0 \text{ or } y^2 < -b, \tag{6}$$

$$u^1 = -\int V(t)\,\mathrm{d}t, \quad T^2 = 0 \quad \text{on } y^1 = -a_i \text{ and } -b \leqslant y^2 \leqslant 0, \tag{7}$$

where in (7)

$$V(t) = \begin{cases} V_1\, t/t_\mathrm{r}, & \text{for } 0 \leqslant t < t_\mathrm{r}, \\ V_1, & \text{for } t_\mathrm{r} \leqslant t \leqslant t_\mathrm{p}, \\ V_1[1 - (t - t_\mathrm{p})/t_\mathrm{s}], & \text{for } t_\mathrm{p} < t < (t_\mathrm{p} + t_\mathrm{s}), \\ 0, & \text{for } t \geqslant (t_\mathrm{p} + t_\mathrm{s}). \end{cases} \tag{8}$$

Here, t_r is the rise time, t_p is the pulse time and t_s is the step down time. In the calculations t_r and t_s are taken to be 0.1 μs. The pulse time and the impact velocity, V_1, is varied.

The specimen consists of the unidirectional fiber-reinforced composite and Homalite, which is isotropic, joined along the bond line $y^2 = 0$, $y^1 > 0$. In Cartesian coordinates, the volumetric elastic constitutive relation for each material can be written in the form

$$S_{11} = L_{11}E_{11} + L_{12}E_{22} + L_{12}E_{33}, \tag{9}$$

$$S_{22} = L_{12}E_{11} + L_{22}E_{22} + L_{23}E_{33}, \tag{10}$$

$$S_{12} = L_{44}E_{12}. \tag{11}$$

In plane stress, (9) and (10) become

$$S_{11} = C_{11}E_{11} + C_{12}E_{22}, \quad S_{22} = C_{12}E_{11} + C_{22}E_{22}, \quad S_{12} = C_{44}E_{12}. \tag{12}$$

Here, the C_{ij} are the plane stress moduli, which are related to the three-dimensional elastic constants L_{ij} via

$$C_{11} = L_{11} - \frac{L_{12}^2}{L_{22}}, \qquad C_{22} = L_{22} - \frac{L_{23}^2}{L_{22}}, \tag{13}$$

$$C_{12} = L_{12} - \frac{L_{12}L_{23}}{L_{22}}, \qquad C_{44} = L_{44}. \tag{14}$$

The longitudinal and shear wave speeds are related to the material properties through the relations:

$$c_l = \sqrt{\frac{C_{11}}{\rho}}, \qquad c_s = \sqrt{\frac{C_{44}}{\rho}}, \tag{15}$$

where ρ is the mass density of the material. For an isotropic elastic material such as Homalite, the relations for the wave speeds become

$$c_l = \sqrt{\frac{E}{\rho(1-\nu^2)}}, \quad c_s = \sqrt{\frac{E}{2\rho(1+\nu)}}. \tag{16}$$

Another characteristic elastic wave speed is the Rayleigh surface wave speed, which for an isotropic elastic material is given by

$$c_R = c_s \frac{0.862 + 1.14\nu}{1+\nu}. \tag{17}$$

A cohesive surface constitutive relation is specified between the tractions and displacement jumps across a single cohesive surfaces that lies along the bond line $y^2 = 0$ in front of the initial crack. The cohesive surface constitutive relation allows for both normal and tangential decohesion, with the normal and shear tractions given by (Xu and Needleman, 1993)

$$T_n = -\frac{\phi_n}{\delta_n} \exp\left(-\frac{\Delta_n}{\delta_n}\right) \left\{ \frac{\Delta_n}{\delta_n} \exp\left(-\frac{\Delta_t^2}{\delta_t^2}\right) + \frac{1-q}{r-1}\left[1 - \exp\left(-\frac{\Delta_t^2}{\delta_t^2}\right)\right]\left[r - \frac{\Delta_n}{\delta_n}\right] \right\}, \tag{18}$$

$$T_t = -\frac{\phi_n}{\delta_n}\left(2\frac{\delta_n}{\delta_t}\right)\frac{\Delta_t}{\delta_t}\left\{q + \left(\frac{r-q}{r-1}\right)\frac{\Delta_n}{\delta_n}\right\} \exp\left(-\frac{\Delta_n}{\delta_n}\right) \exp\left(-\frac{\Delta_t^2}{\delta_t^2}\right), \tag{19}$$

where $\Delta_n = \mathbf{n}\cdot\boldsymbol{\Delta}$, $\Delta_t = \mathbf{t}\cdot\boldsymbol{\Delta}$, $T_n = \mathbf{n}\cdot\mathbf{T}$ and $T_t = \mathbf{t}\cdot\mathbf{T}$ with $\mathbf{n}$ and $\mathbf{t}$ as the normal and tangent, respectively, to the surface at a given point in the reference configuration. Also, $q = \phi_t/\phi_n$ and $r = \Delta_n^*/\delta_n$, where Δ_n^* is the value of Δ_n after complete shear separation with normal traction $T_n = 0$ ($r = 0$ in all calculations here). The normal work of separation, ϕ_n, and the shear work of separation, ϕ_t, can be written as

$$\phi_n = \mathrm{e}\sigma_{\max}\,\delta_n \qquad \phi_t = \sqrt{\frac{e}{2}}\,\tau_{\max}\,\delta_t. \tag{20}$$

Here, $\mathrm{e} = \exp(1)$, $\sigma_{\max}$ and $\tau_{\max}$ are the cohesive surface normal strength and tangential strength, respectively, and δ_n and δ_t are corresponding characteristic lengths. The tractions in (18) and (19) are derived from a potential and the sign convention is that restoring tractions are positive. For normal separation, the maximum value of $-T_n$ is $\sigma_{\max}$ and occurs when $\Delta_n = \delta_n$; in shear, the maximum value of $|T_t| = \tau_{\max}$ is attained when $|\Delta_t| = \sqrt{2}\delta_t/2$.

The finite element discretization is based on linear displacement triangular elements that are arranged in a 'crossed-triangle' quadrilateral pattern. The mesh used, which

is the same as in Needleman and Rosakis (1999), has 61,312 quadrilateral elements and 247,424 degrees of freedom, with a uniform region in front of the initial crack of 400×8 rectangular quadrilateral elements. Each rectangle in the uniform region is 75 μm × 100 μm, so that the uniform mesh extends 30 mm in front of the initial crack tip, and the mesh spacing is gradually increased in size out to the boundary. The equations of motion that result from substituting the finite element discretization into (2) are integrated numerically by an explicit integration procedure, the Newmark β-method with $\beta = 0$, Belytschko et al. (1976). A lumped mass matrix is used instead of the consistent mass matrix, since this has been found preferable for explicit time integration procedures, from the point of view of accuracy as well as computational efficiency, Krieg and Key (1973).

4. Results

The three loading configurations sketched in Fig. 2 are considered both in the experiments and the computations:

Case 1. Impact of the composite on the cracked edge.
Case 2. Impact of the Homalite on the cracked edge.
Case 3. Impact of the composite on the edge opposite the initial crack.

In reporting the results, crack speeds are compared to various elastic wave speeds; in particular, the Rayleigh wave speed of Homalite, $c_R^H = 1155$ m/s (the surface wave speed of the more compliant material); the longitudinal wave speed of Homalite, $c_l^H = 2187$ m/s (the body wave speed for the more compliant material); and the longitudinal wave speed of the composite, $c_l^c = 7380$ m/s (the body wave speed parallel to the bond line for the stiffer material). For this purpose, the plane stress longitudinal wave speeds in (15) and (16) are used. In addition, $\sqrt{2}c_s^H = 1775$ m/s is also used as a reference wave speed. For homogeneous Homalite, this is the only intersonic shear crack speed at which, according to singular theories of dynamic fracture (Freund, 1979), there is a finite energy release rate. However, for the bimaterial problem it has no known energetic significance. Nonetheless, it is worth noting that this speed plays a special role in the analysis of isotropic elastic-rigid bimaterial systems, Lambros and Rosakis (1995), Liu et al. (1995). In such systems, $\sqrt{2}c_s$ is the crack speed at which the crack opening displacement behind the intersonically traveling shear crack vanishes, regardless of the sign or magnitude of the far field loading. At intersonic shear crack speeds above or below $\sqrt{2}c_s$, an asymptotic analysis of singular crack tip fields, Liu et al. (1995), predicts either opening or closing, depending on the sign of shear.

For bimaterial systems, various characteristic interface waves may exist. For example, for isotropic solids, generalized Rayleigh waves and Stoneley waves may be available. For anisotropic solids, an even richer set of interface waves become possible, Barnett et al. (1988). The composite–Homalite bimaterial system has the unusual feature of having a small shear wave speed mismatch and a large longitudinal wave speed mismatch. Interface waves possible for this anisotropic system have not been computed. However, to give an indication of the possible range for the generalized Rayleigh wave speed,

Table 2
Projectile impact velocity, time to crack initiation after impact and sustained crack speed attained in the experiments

Case	Impact velocity (m/s)	Initiation time (μs)	Sustained crack speed (m/s)
Case 1	40	8	7500
Case 1	35	8	6500
Case 1	27	4	6000
Case 2	22	35	1820
Case 2	30	41	1240
Case 2	24	32	1290
Case 2	28	31	1800
Case 2	40	35	1830
Case 3	27	30	2080
Case 3	43	33	2150

it was calculated from the isotropic expression, e.g. Weertman (1963) and Achenbach and Epstein (1967), using the values of both $c_c^{\|}$ and $c_c^{\perp}$ for c_l^c. With c_l^c identified with $c_c^{\|}$, the generalized Rayleigh wave speed is 1260 m/s and it is 1245 m/s when c_l^c is identified with $c_c^{\perp}$, suggesting that there is no strong dependence on the anisotropy for this system.

4.1. Experimental results

The impact velocity, the time to crack initiation after impact and the sustained crack speed attained in the experiments are summarized in Table 2.

4.1.1. Case 1

Initially, a steel plate was used at the impact site with the edge of the impact 25 mm below the bond line and, in these experiments, the crack kinked into the Homalite half of the specimen. In order to increase the relative amount of shear and promote interfacial crack growth, the edge of the impact was shifted to the bond line. This succeeded in suppressing the kinking of a mode I crack into the Homalite.

Successful interfacial crack growth experiments were carried out with impact velocities of 27, 35 and 40 m/s. A typical sequence of isochromatic fringe patterns is shown in Fig. 3 for an impact velocity of 35 m/s. The field of view, which is in the Homalite, is approximately a semicircle with a diameter of 100 mm. Two sets of fringes are observed (shown with arrows in Fig. 3). The first set of fringes are the broad fringes that emanate from the wave front and make an angle of 17° with bond line. The second set of fringes have finer spacing at a shallower angle of 10° to the bond line. These two sets of fringes correspond to the longitudinal and shear head waves, respectively, due to the impact wave front traveling at 7380 m/s in the composite. The set of fringes corresponding to the shear head wave is disrupted by

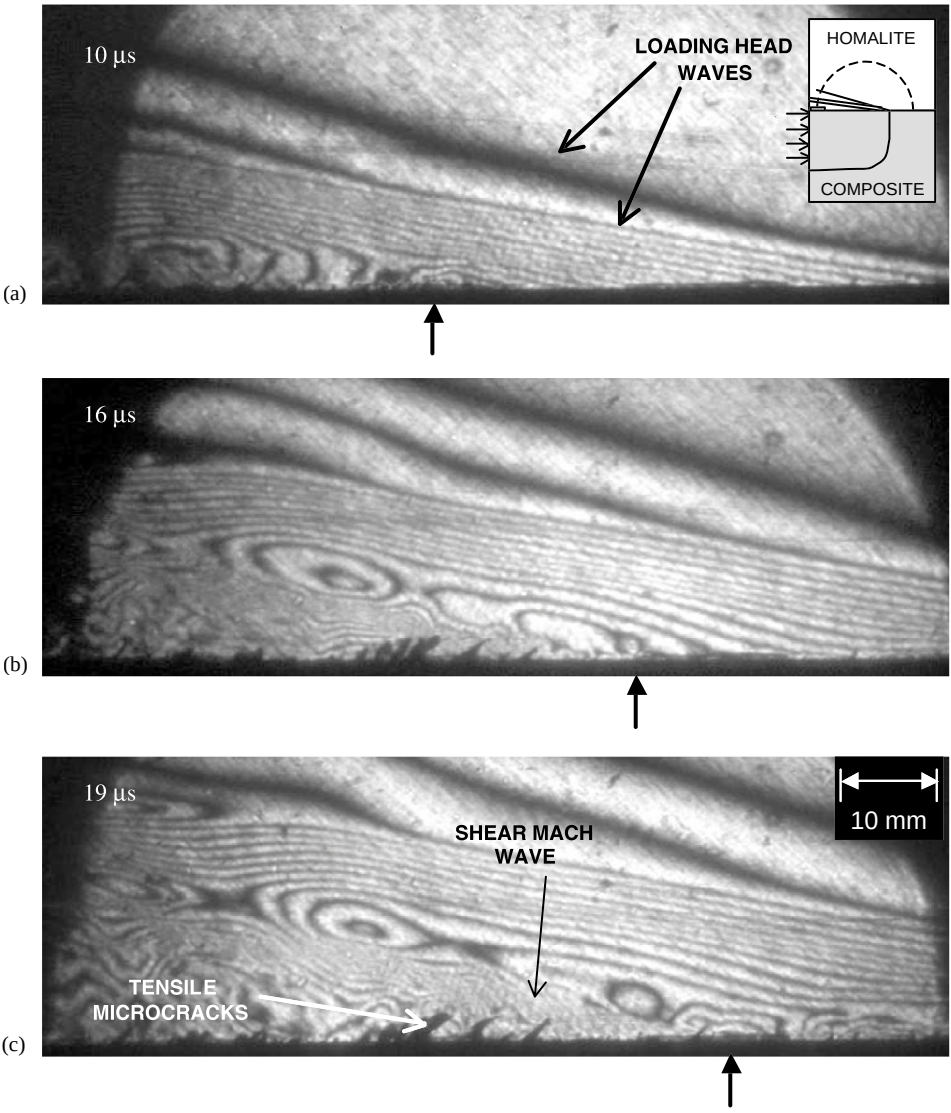

Fig. 3. A sequence of isochromatic fringe patterns showing interfacial supersonic crack propagation for case 1 with an impact velocity of 35 m/s. The inset in (a) illustrates the loading configuration.

a region of vortical fringe patterns, after which a set of parallel fringes with a finer spacing are observed closer to the bond line at an angle of approximately 11° to the bond line. These fringes are Mach waves indicating the presence of a disturbance on the interface, with a stress concentration, traveling at a speed of about 6500 m/s. The disturbance creating this band of fringes is consistent with a crack tip traveling at a supersonic speed (relative to the Homalite) following the loading wave which travels at

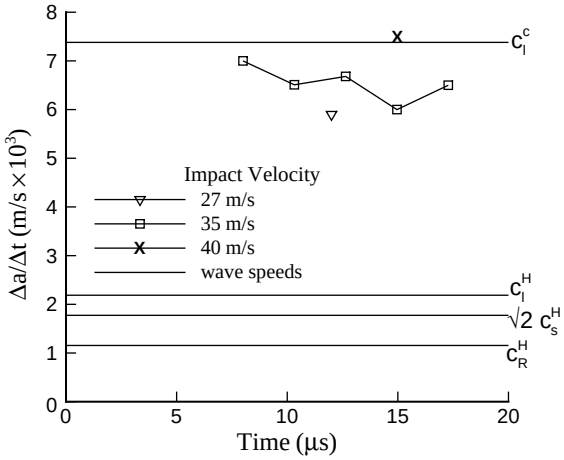

Fig. 4. Experimentally determined crack speeds, $\Delta a/\Delta t$, versus time for case 1.

c_l^c. Behind these fringes protrusions from the bond line are observed at an angle of approximately 30° to the vertical (see Fig. 3b). Post-mortem observations of the Homalite show that these are associated with secondary mode I micro-cracks emanating from the interface into the Homalite. Similar secondary cracks were observed previously in experiments on bonded homogeneous Homalite–Homalite systems (Rosakis et al., 2000) trailing an intersonically growing shear crack and were analyzed by Samudrala et al. (2002).

The crack speed, $\Delta a/\Delta t$, is determined from the slope of measured crack extension Δa versus time data extracted from a sequence of photographs by using a progressive three-point least-squares method. The inferred crack speed as a function of time is plotted in Fig. 4, with the most data points obtained for an impact velocity of 35 m/s. For all three impact velocities, the sustained crack speed is well above the longitudinal wave speed of Homalite (2200 m/s) and is just below the longitudinal wave speed of the composite, i.e. the crack speed is supersonic with respect to the Homalite.

4.1.2. Case 2

In Fig. 5, a sequence of isochromatic fringe patterns around the crack tip is shown for a specimen impacted on the Homalite side at 40 m/s. The progress of the compressional loading wave front in the Homalite can be observed (indicated with an arrow in Fig. 5a). A steel plate was bonded to the specimen when impacting the Homalite in order to prevent the Homalite from shattering. As a consequence of impact occurring on the steel plate, the edge of impact is 25 mm below the notch line and the loading wave in Fig. 5a is not perfectly vertical. Part of the loading is transferred across the bond line into the composite where the higher elastic wave speed induces a head wave in Homalite (single dark band close to the interface in Figs. 5a and b) which propagates ahead of the loading wave front.

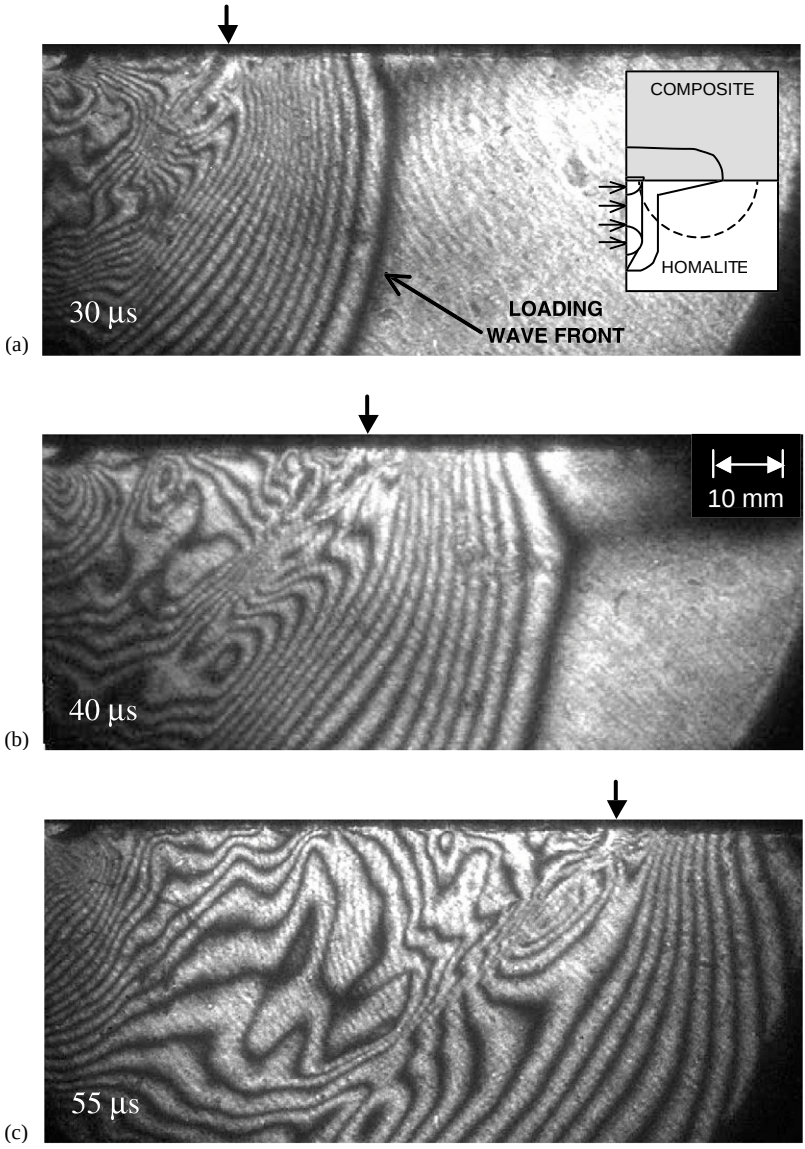

Fig. 5. A sequence of isochromatic fringe patterns showing interfacial intersonic crack growth and the corresponding shear shock front for case 2 with an impact velocity of 40 m/s. The inset in (a) illustrates the loading configuration.

The location of the crack tip at each time is shown with an arrow in Figs. 5a–c. The photoelastic fringe pattern around the crack has a characteristic set of features observed for dynamically growing cracks at intersonic speeds (Singh and Shukla, 1996; Rosakis et al., 2001). A shear Mach wave, radiating from the crack tip at an angle

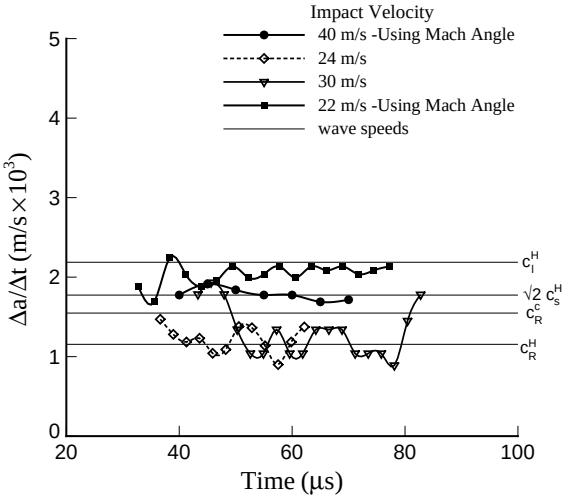

Fig. 6. Experimentally determined curve of crack speed, $\Delta a/\Delta t$, versus time for case 2 with various impact velocities. The solid symbols denote crack speeds calculated using the Mach formula (21).

of approximately 45° is seen which signifies that the crack is moving faster than the shear wave speed of Homalite.

The crack speed is shown as a function of time for four experiments in Fig. 6. Two methods were used to calculate the crack tip speed. In addition to the progressive three-point least-squares method used to determine $\Delta a/\Delta t$ from the crack extension history (obtained from a sequence of photographs), the relation between the crack speed and the Mach angle is used to calculate the crack speed from

$$\sin\theta = c_s/(\Delta a/\Delta t) \tag{21}$$

in cases where the crack propagates faster than the shear wave speed of Homalite. The crack speeds in Fig. 6 calculated as $\Delta a/\Delta t$ are shown as open symbols and those calculated from the Mach angle as closed symbols.

For the case shown in Fig. 6 with an impact velocity of 40 m/s, the sustained crack speed is approximately $\sqrt{2}c_s^H$. For lower impact velocities, 24 and 30 m/s, the sustained crack speed is in the neighborhood of c_R^H. With an impact velocity of 22 m/s the crack speed approaches c_I^H. This apparent inconsistency (higher crack speed with a lower impact velocity) is attributed to the weaker interface bond for this specimen. Thus, within experimental error, sustained crack speed regimes for case 2 are found to be about c_R^H for lower impact velocities and to approach c_I^H for larger impact velocities or weaker bonds.

4.1.3. Case 3

A time sequence of photographs is shown in Fig. 7 for an impact velocity of 27 m/s where the notch tip is on the lower left corner of the field of view. As the loading wave approaches (from the right-hand side in Fig. 7) and passes the crack tip it loads the

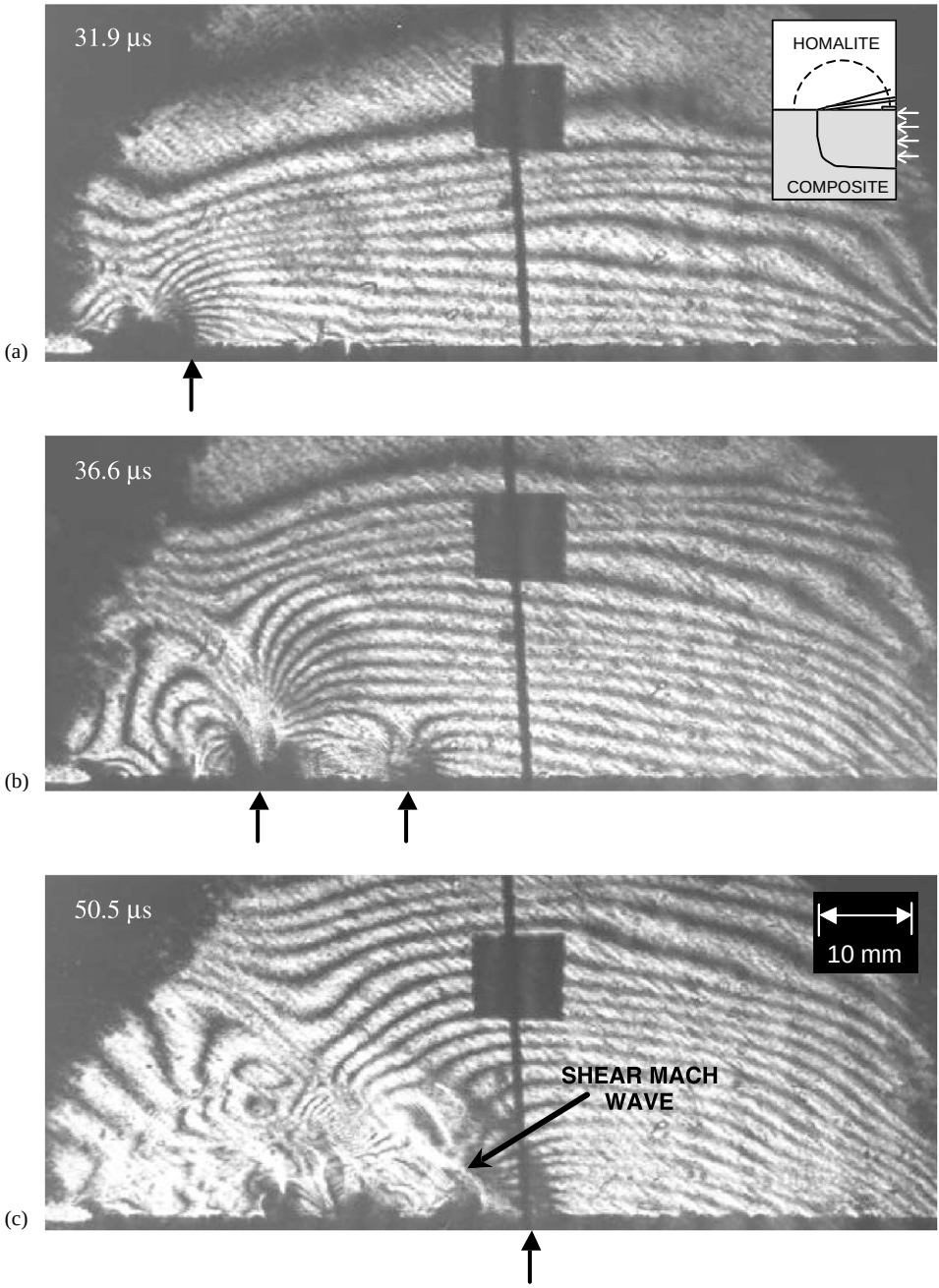

Fig. 7. A sequence of isochromatic fringe patterns for case 3 with 27 m/s, showing the mother–daughter crack growth mechanism. The inset in (a) illustrates the loading configuration.

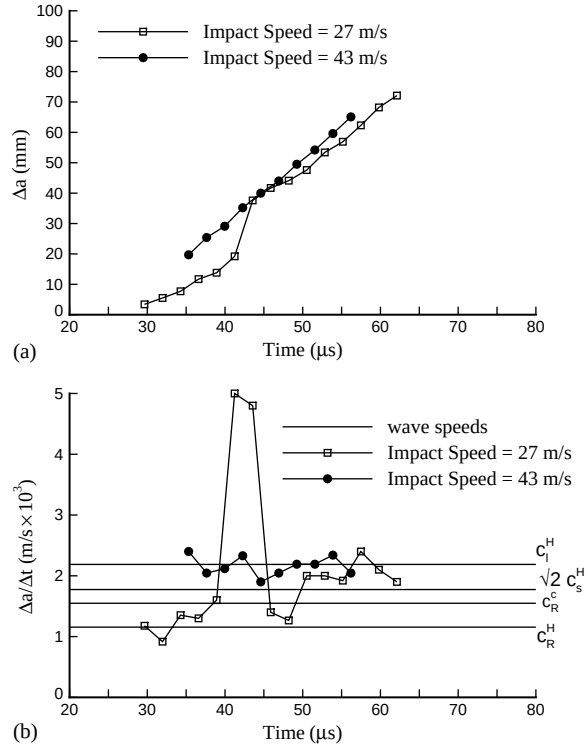

Fig. 8. Experimentally determined curves of (a) crack extension, Δa and (b) crack speed, $\Delta a/\Delta t$, as a function of time for case 3.

crack primarily in shear. In Fig. 7a, which is at 30 μs after impact, the crack has just initiated after the loading wave has reflected off the opposite free surface doubling the particle velocity. The crack propagates from the notch tip at 1100 m/s, which is close to the Rayleigh wave speed of the Homalite. In Fig. 7b, a daughter crack nucleates in front of the main crack. The arrows indicate the location of the main crack tip and the daughter crack. Subsequently, the main crack and the daughter crack coalesce and travel at a crack speed of ≈ 2100 m/s with a corresponding shear shock wave attached to the moving shear crack tip (Fig. 7c).

Evidence for this process is also seen in Fig. 8 where the position of the crack tip and the crack speed are plotted as functions of time. For an impact velocity of 27 m/s, a crack speed of about c_R^H is maintained until there is a jump in crack length (Fig. 8a) and a corresponding jump in crack speed at about 40 μs (Fig. 8b). Subsequently the crack maintains a speed close to c_I^H. The mechanism of daughter crack nucleation to attain intersonic crack speeds has been seen in theoretical and computational analyses of bimaterials consisting of two identical homogeneous isotropic solids bonded together; Burridge (1973), Andrews (1976), Needleman (1999), Abraham and Gao (2000), Geubelle and Kubair (2001) and Abraham (2001). Abraham (2002) has also carried out molecular dynamics calculations for bonded solids whose linearized

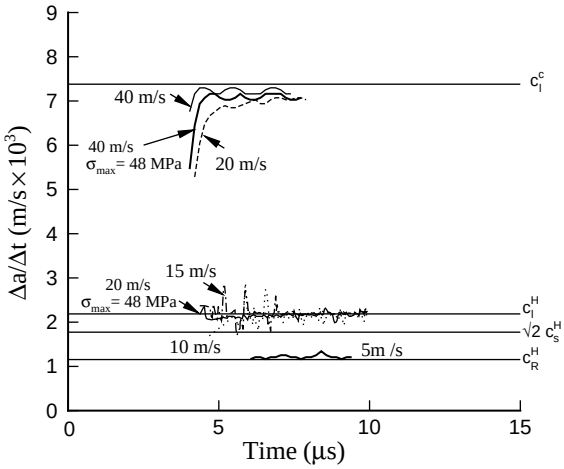

Fig. 9. Numerically computed curves of crack speed, $\Delta a/\Delta t$, versus time for case 1 with various impact velocities. Unless indicated otherwise, $\sigma_{\max} = 24$ MPa. In all calculations, $t_p = 25$ μs.

behavior is identical but that exhibit different nonlinear behaviors. For this system, the occurrence of a mother–daughter crack mechanism was found that was very similar to that for a strictly homogeneous bonded system. However, to our knowledge, our results provide the first direct experimental observation of the mother–daughter mechanism, albeit for a bimaterial where one of the constituents is not isotropic. Also shown in Fig. 8 are results for an impact velocity of 43 m/s which are denoted by solid symbols. For this impact velocity, the crack accelerates directly to a speed of about c_l^H, at least within the time resolution of the experiments.

4.2. Numerical results

Unless specifically stated otherwise, the parameters characterizing the cohesive surface are $\sigma_{\max} = \tau_{\max} = 24$ MPa, which is an estimate of the static strength of the adhesive and is half the static tensile strength of Homalite in Table 1, $\delta_n = 0.4$ μm and $\delta_t = 0.9327$ μm (the same values of δ_n and δ_t as in Needleman and Rosakis, 1999) giving $\phi_n = \phi_t = 26.1$ J/m^2. In (8), impact velocities V_1 ranging from 5 to 50 m/s are considered and the pulse width, t_p in (8), is varied from 3 to 25 μs. Calculations are terminated before the crack reaches the end of the fine mesh region and the time for this to occur did not exceed 25 μs in any of the calculations. For the composite, we take $L_{11} = 82$ GPa, $L_{12} = 4$ GPa, $L_{22} = 11.1$ GPa, $L_{23} = 4.9$ GPa and $L_{44} = 3.1$ GPa in (9)–(11). The density of the composite as well as the density and elastic properties of the isotropic Homalite are as specified in Table 1.

4.2.1. Case 1

Fig. 9 shows curves of crack speed versus time for impact velocities of 5, 10, 15, 20 and 40 m/s with the pulse width, t_p, fixed at 25 μs. For comparison purposes, two

calculations in Fig. 9 are carried out for a stronger bond having $\sigma_{\max} = \tau_{\max} = 48$ MPa. The first step in computing the crack speed is to record the crack location, which is defined by the position of the furthest node from the initial crack tip where Δ_t is greater than or equal to $5\delta_t$. This gives the crack position at various times and the crack speed is then calculated from this data by a progressive least-squares fit using five points. In the following, $\Delta a/\Delta t$ denotes the instantaneous crack speed so calculated, while the phrase "sustained crack speed" is used to refer to the value of a more or less steady crack speed.

Three discrete levels of sustained crack speed are attained as the impact velocity varies: (i) a crack speed of approximately c_R^H; (ii) a crack speed near c_l^H; and (iii) a crack speed about c_l^c. The time to the initiation of crack growth decreases with increasing impact velocity, with the difference in initiation time between the calculations with impact velocities of 5 and 50 m/s being 2 μs. For the calculation with a bond strength of 48 MPa and an impact velocity of 20 m/s, the sustained crack speed is about c_l^H. Thus, the effect of a stronger bond is to increase the impact velocity at which the sustainable crack speed reaches the next attainable regime. Similar crack speed transitions were found in Needleman and Rosakis (1999) and Needleman (1999).

Fig. 10 shows numerically computed isochromatic fringe patterns, which are contours of $(\sigma_1 - \sigma_2)$, where σ_1 and σ_2 are the maximum and minimum principal Cauchy stresses, respectively, at 6 μs after impact at which time the loading wave has propagated 20 mm. The sustained crack speeds are about c_l^c in Fig. 10a, about c_l^H in Fig. 10b and about c_R^H in Fig. 10c. The head wave in Homalite emanating from the wave front in the composite, with a slope corresponding to the longitudinal wave speed of Homalite is seen in all three plots. The finer fringes emanating from the loading wave in Figs. 10a and b (shear head waves) arise because the loading in the composite is faster than c_s^H. In Fig. 10a, there is a higher density of fringes inclined at an angle of 11° immediately behind the shear head waves, due to the presence of a crack (shown with an arrow) traveling faster than the shear wave speed of Homalite. This set of fringes reflects the shear Mach wave emanating from the crack tip across which there are steep stress gradients. The calculated fringe patterns in Fig. 10a are in excellent agreement with the experimental fringe pattern shown in the inset (also see Fig. 3). In Fig. 10b, with $V_1 = 15$ m/s, the sustained crack speed is $\approx c_l^H$ and the crack trails the loading wave front. The crack tip locations (defined by the furthest distance from the origin at which $\Delta_t = 5\delta_t$ and shown by the arrows in Fig. 10) are at 13.8 and 4.8 mm in Figs. 10a and b, respectively. With $V_1 = 5$ m/s (Fig. 10c) $t = 6$ μs corresponds to a time shortly after the initiation of crack growth and $\Delta a = 0.45$ mm.

Contours of S_{22} for the three crack speed regimes are shown in Fig. 11 at $t = 6$ μs. The stresses are compressive in front of the supersonically propagating crack (a crack speed greater than c_l^H), Fig. 11a, whereas for an intersonically propagating crack (a crack speed between c_s^H and c_l^H) there are tensile opening stresses immediately in front of the crack tip, Fig. 11b. Alternating positive and negative normal stresses occur in Fig. 11a behind the crack above the crack faces. These features are also observed in the experiments (see Fig. 3). The computed isochromatic fringe pattern in Fig. 11c,

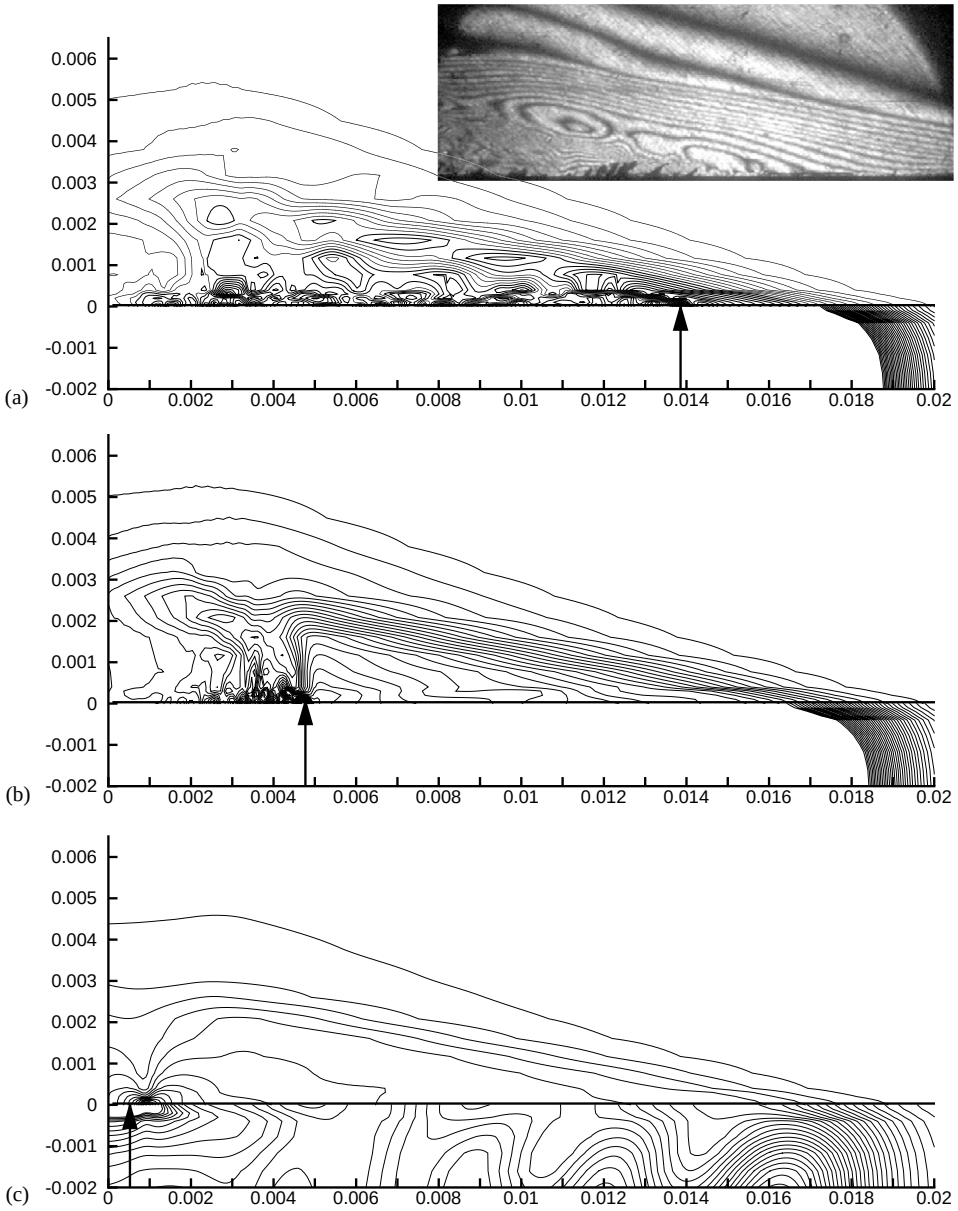

Fig. 10. Computed isochromatic fringe patterns (contours of $\sigma_1 - \sigma_2$) at 6 μs for case 1. (a) $V_1 = 20$ m/s; $\Delta a/\Delta t = 6980$ m/s. (b) $V_1 = 15$ m/s; $\Delta a/\Delta t = 2170$ m/s. (c) $V_1 = 5$ m/s; $\Delta a/\Delta t = 1170$ m/s. The arrows show the current crack tip location and lengths marked on the axes are in m. For comparison purposes, the experimental fringe pattern from Fig. 3b is shown in the inset in (a).

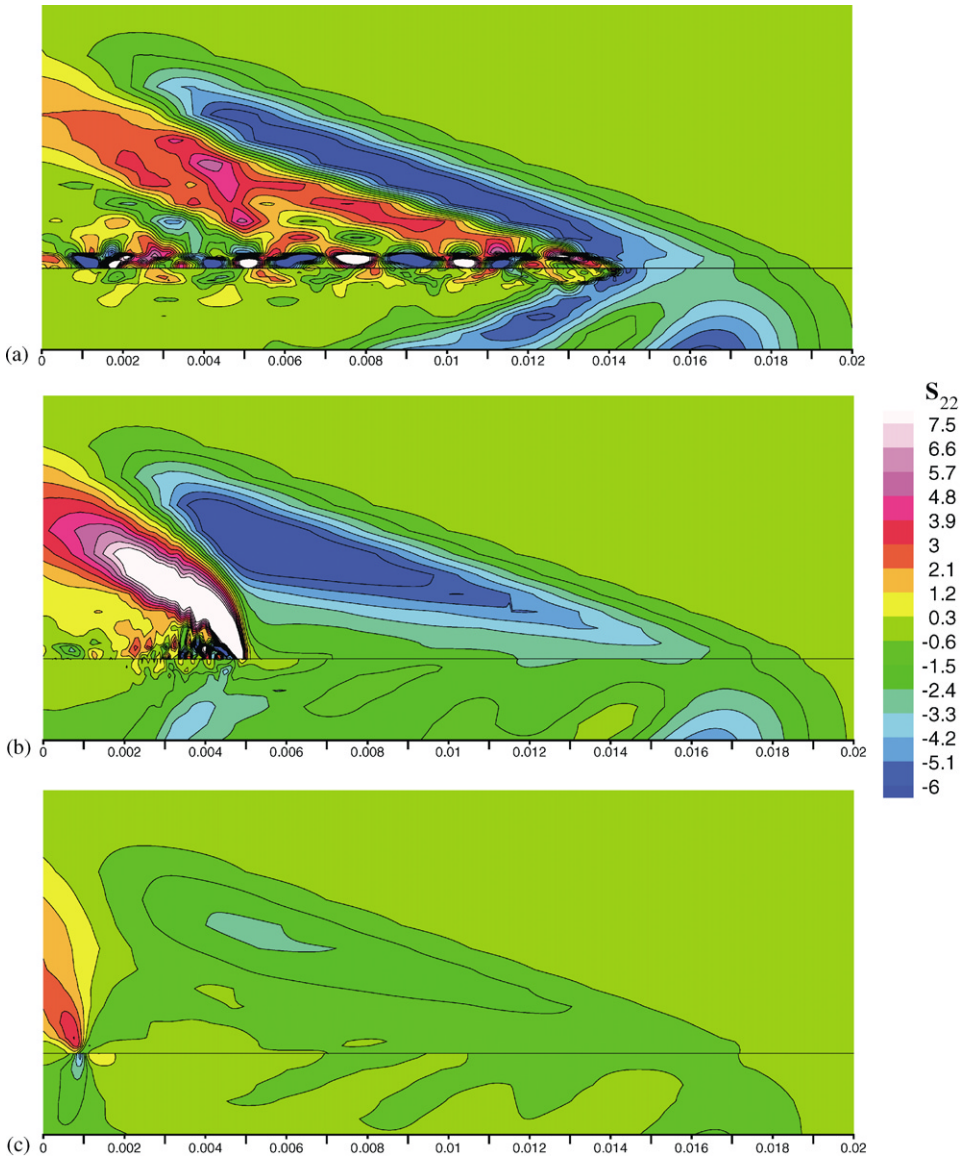

Fig. 11. Contours of S_{22} for case 1 at 6 μs. (a) $V_1 = 20$ m/s; $\Delta a/\Delta t = 6980$ m/s; $\Delta a = 13.9$ mm. (b) $V_1 = 15$ m/s; $\Delta a/\Delta t = 2170$ m/s; $\Delta a = 4.8$ mm. (c) $V_1 = 5$ m/s; $\Delta a/\Delta t = 1170$ m/s; $\Delta a = 0.9$ mm. The crack tip locations are as shown in Fig. 10. Lengths marked on the axes are in m.

where the crack speed is about c_R^H, is of the type typically observed experimentally for a subsonically moving crack in a bimaterial, Rosakis et al. (1998).

The normal traction and the normal displacement jump along the bond line are plotted for a supersonically propagating crack in Fig. 12a, for an intersonically propagating

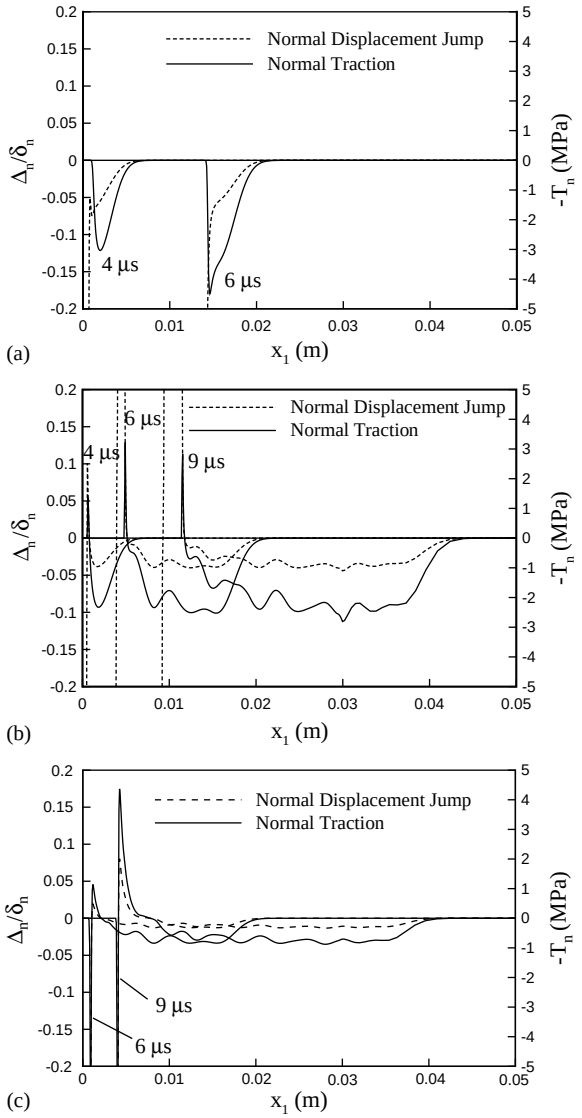

Fig. 12. Normal traction, T_n, and displacement jump, Δ_n, along the crack line ($y^2 = 0$) for case 1. (a) $V_1 = 20$ m/s; $\Delta a/\Delta t = 6980$ m/s, showing a crack-like distribution. (b) $V_1 = 15$ m/s; $\Delta a/\Delta t = 2170$ m/s, showing a pulse-like distribution. (c) $V_1 = 5$ m/s; $\Delta a/\Delta t = 1170$ m/s, showing a pulse-like distribution.

crack in Fig. 12b and for a crack propagating at about c_R^H in Fig. 12c. Here, $-T_n$ is plotted so that negative values correspond to compression. In Fig. 12a, where $V_1 = 20$ m/s and the crack speed is about c_1^c, T_n and Δ_n exhibit distributions that correspond to a crack-like propagation mode. The value of the traction monotonically increases

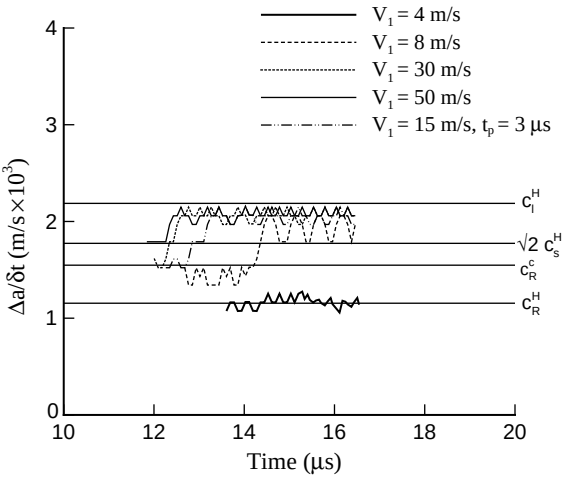

Fig. 13. Numerically computed curves of crack speed, $\Delta a/\Delta t$, versus time for case 2 with various impact velocities. Unless indicated otherwise, $t_p = 25$ μs.

along the bond line as the crack tip is approached, reaching a maximum value near the crack tip. However, in Figs. 12b (where $V_1 = 15$ m/s and the crack speed is about c_l^H) and c (where $V_1 = 5$ m/s and the crack speed is about c_R^H) there is an expanding compressive pulse-like distribution of Δ_n and T_n ahead of the crack. In addition, there is a propagating opening pulse of Δ_n behind the crack tip. Neither Δ_t nor T_t exhibit pulse-like behavior. To give an indication of where the crack tip is relative to the features in Fig. 12, $\Delta a = 14.0$ mm at $t = 6$ μs in Fig. 12a, $\Delta a = 11.4$ mm at $t = 9$ μs in Fig. 12b and $\Delta a = 3.4$ mm at $t = 9$ μs in Fig. 12c.

4.2.2. Case 2

Curves of crack speed versus time for various values of impact velocity V_1 and with the pulse duration t_p fixed at 25 μs are shown in Fig. 13. For an impact velocity of 4 m/s, the sustained crack speed is c_R^H. When the impact velocity is increased to 8 m/s, the sustained crack speed is initially c_R^c, or smaller, but then rather abruptly increases to a level close to c_l^H. The time at which the abrupt increase in sustained crack speed occurs varies with the impact conditions and is not obviously correlated with the arrival of any reflected wave. Even when the impact velocity is 50 m/s with a pulse duration of 25 μs, the sustained crack speed does not exceed c_l^H. Additional calculations (not shown) were carried out with the pulse width varying between 5 and 25 μs, and the sustainable crack speed regimes did not change with pulse width.

Isochromatic fringe patterns are shown in Fig. 14a for a crack propagating at c_l^H ($V_1 = 30$ m/s) and in Fig. 14b for a crack propagating at c_R^H ($V_1 = 5$ m/s). In both plots, the time is 15 μs after impact. In Fig. 14a the crack is propagating at an intersonic speed with respect to both the composite and Homalite shear wave speeds. Shear Mach

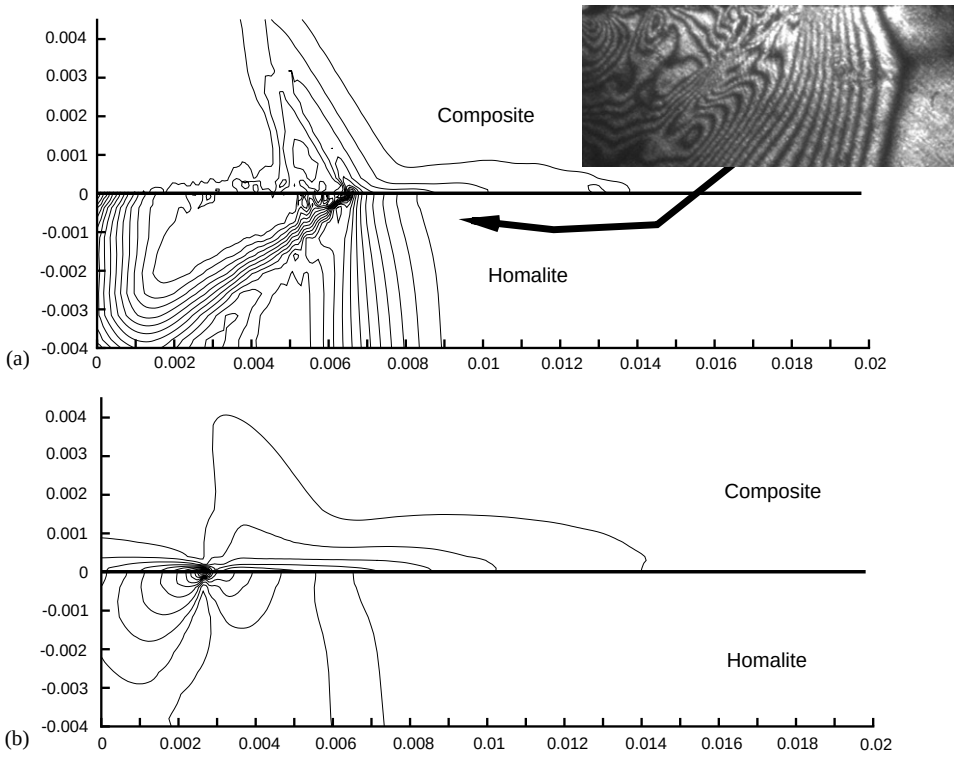

Fig. 14. Computed isochromatic fringe patterns (contours of $\sigma_1 - \sigma_2$) at 6 μs for case 2. (a) $V_1 = 30$ m/s; $\Delta a/\Delta t = 2090$ m/s. (b) $V_1 = 4$ m/s; $\Delta a/\Delta t = 1230$ m/s. For comparison purposes, the experimental fringe pattern from Fig. 5b is shown in the insert in (a). Lengths marked on the axes are in m.

waves are seen in both the composite and Homalite, with the fringes lined up along two oblique lines in the bottom and the top with slopes corresponding to the shear wave speed of the composite and Homalite. This is in contrast to the fringe pattern observed in Fig. 14b for a crack propagating at c_R^H, i.e., subsonically. For all calculations in Fig. 13, the opening stresses immediately ahead of the crack tip are compressive, i.e. $S_{22} < 0$.

Fig. 15 shows the normal and shear tractions along the crack line for the same two cases. Very close to the crack tip the stresses increase monotonically for both calculations. However, further ahead of the crack tip, there are oscillations in the normal traction for $\Delta a/\Delta t = 2090$ m/s (Fig. 15a). With $\Delta a/\Delta t = 1230$ m/s the oscillations are much smaller in amplitude (Fig. 15b). The oscillations occur in Δ_n but not in Δ_t and, as a consequence, the oscillations are not as visible in the distribution of T_t. Each half-wave in the oscillations is approximately 1.5 mm, encompassing about 20 mesh points, and, hence, are well resolved by the discretization. The oscillations are consistent with the predictions of complex singularity exponents at the tip of intersonically growing cracks in elastic bimaterials. In these predictions, the complex or real nature

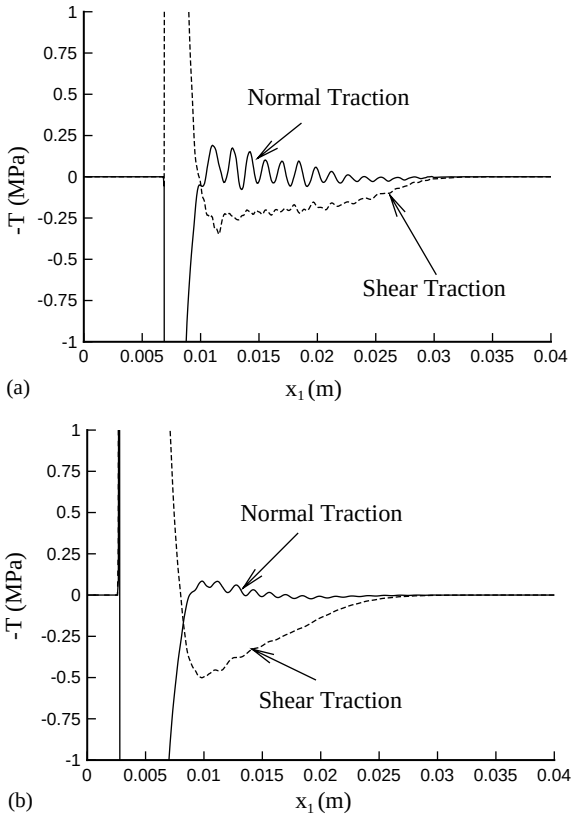

Fig. 15. Normal tractions and displacements along the crack line for case 2 at time = 15 μs. (a) $V_1 = 50$ m/s; $\Delta a/\Delta t = 2090$ m/s, (b) $V_1 = 4$ m/s; $\Delta a/\Delta t = 1230$ m/s.

of the singularity exponent depends on the shear wave speed mismatch and on the crack speed, Huang et al. (1998).

4.2.3. Case 3

Crack speed histories for case 3 are shown in Fig. 16. In each calculation, crack growth initiated just after the impact wave front passed the initial crack tip at around 14 μs. The crack is loaded a second time at ≈ 21 μs when the wave is reflected from the notched end of the specimen and catches up with the growing crack tip. Before the reflected wave reaches the crack tip, the stress state ahead of the crack tip is one of shear and tension; after the reflected wave has caught up with the crack tip, the stress state ahead of the crack changes to shear and compression as in case 1. A crack speed transition, or attempted crack speed transition, is associated with the reflected wave reaching the crack tip.

In Fig. 16a, the crack speed is plotted as a function of time for loading pulse widths of 25 and 3 μs and for impact velocities of 10, 15 and 20 m/s. In all calculations in

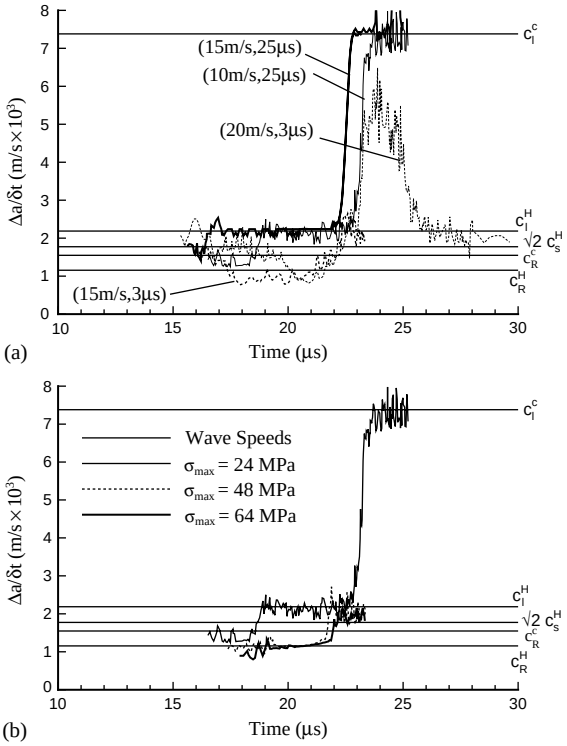

Fig. 16. Numerically computed curves of crack speed, $\Delta a/\Delta t$, versus time for case 2. (a) Effect of impact velocity, V_1, and pulse width, t_p, shown as (V_1, t_p) with $\sigma_{max} = 24$ MPa. (b) Effect of cohesive strength, σ_{max}, with $V_1 = 10$ m/s and $t_p = 25$ μs.

Fig. 16a, there is a rather abrupt increase in crack speed at ≈ 22 μs when the reflected impact wave reaches the current crack tip region. The crack speed increases to c_l^c in the two calculations with $t_p = 25$ μs. For a lower impact velocity of 10 m/s, with a pulse width of 25 μs, the crack speed follows a similar trend under the influence of the reflected impact wave, but then slows down to a sustained speed between c_l^H and $\sqrt{2}c_s^H$. With $V_1 = 15$ m/s and $t_p = 3$ μs, the crack speed only slightly exceeds c_l^H at $t \approx 22$ μs, before reaching a sustained speed between c_l^H and $\sqrt{2}c_s^H$. This behavior suggests that the sustained crack speed regime greater than c_l^H involves a crack speed near c_l^c and sufficient energy needs to be supplied to the crack tip for that transition to be made. Fig. 16a also indicates that the sustainable crack speed is strongly dependent on the magnitude and duration of the applied loading and on arrival of the reflected loading wave at the crack tip, consistent with the results in Needleman (1999) for a homogeneous material. Another rather abrupt increase in crack speed occurs in Fig. 16a for the calculation with $V_1 = 15$ m/s and $t_p = 25$ μs at about 16 μs and for the calculation with $V_1 = 10$ m/s and $t_p = 25$ μs at about 18 μ. In both cases, the sustained crack speed increases from below $\sqrt{2}c_s^H$ to c_l^H.

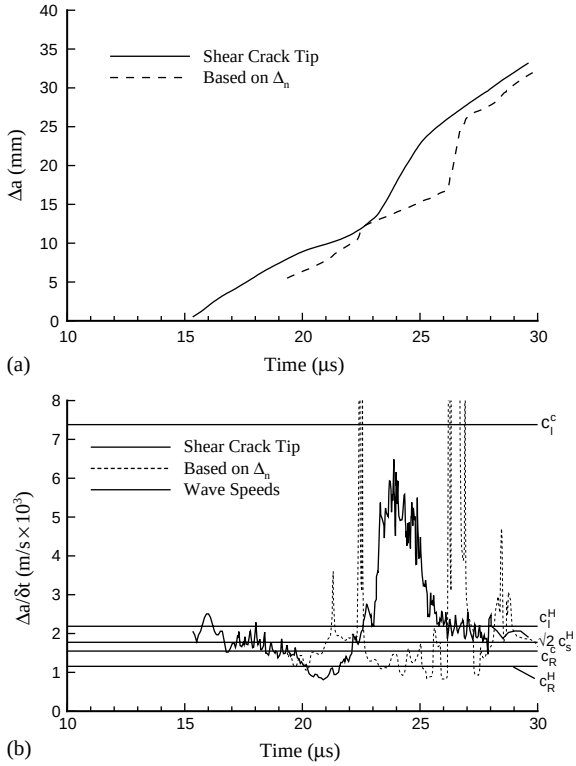

Fig. 17. Numerically computed curves of (a) crack extension, Δa and (b) crack speed, $\Delta a/\Delta t$, as a function of time for case 3 with $V_1 = 20$ m/s and $t_p = 3$ μs. The dotted lines are based on $\Delta_n = 5\delta_n$. Since this point lies behind the shear crack tip, it does not correspond to a crack tip.

The effect of bond strength on crack speed is shown in Fig. 16b for an impact velocity of 10 m/s and a pulse width of 25 μs. Three bond strengths are shown: 24, 48 and 64 MPa. With $\sigma_{max} = 24$ MPa, the initial stages of crack growth take place at a sustained speed between c_R^H and c_R^c. Around 18 μs the sustained crack speed rather abruptly increases to c_l^H (a similar transition to that seen for case 1 in Fig. 13) until a reflected wave arrives at 22 μs when the sustained crack speed jumps to about c_l^c. As the bond strength is increased the crack speed at initiation is decreased and the time for initiation is increased. For both $\sigma_{max} = 48$ MPa and $\sigma_{max} = 64$ MPa, the crack speed transition associated with the arrival of the reflected wave is to a sustained crack speed between $\sqrt{2}c_s^H$ and c_l^H. In the calculations for the stronger bonds, as in the experiments (Fig. 8), sustained supersonic crack speeds are not obtained.

Figs. 17a and b show the crack length and crack speed history, respectively, for $V_1 = 10$ m/s and $t_p = 25$ μs. Two lengths are defined; one associated with Δ_t reaching a specified value and the other with Δ_n reaching a specified value. The crack length corresponds to Δ_t reaching $5\delta_t$. The shear crack speed exceeds c_l^H (i.e., becomes supersonic) at around 23 μs and falls below c_l^H at ≈ 26 μs. Another interesting feature

in Fig. 17 is the existence of a normal opening displacement tip that follows the shear crack tip. At 22.7 μs the opening displacement tip is located at the shear crack tip. At 24.4 μs the shear crack tip leaves the opening displacement jump tip, which is traveling at c_R^H, behind. Subsequently, at ≈ 26 μs, the tip of the opening displacement jump nearly catches up to the shear crack tip. A trailing opening displacement tip was also observed in the atomistic simulations of Abraham and Gao (2000) behind an intersonically moving shear crack tip following the transition from a subsonic to intersonic crack growth.

The mechanism that facilitates this crack speed transition is the creation of a daughter crack ahead of the main crack as seen in Fig. 18. Numerically generated isochromatic fringe patterns, contours of $(\sigma_1 - \sigma_2)$, are plotted at $t = 19.0$ μs ($\Delta a/\Delta t = 1370$ m/s), and $t = 21.0$ μs ($\Delta a/\Delta t = 890$ m/s), which are before the transition, and at $t = 22.9$ μs ($\Delta a/\Delta t = 2470$ m/s) and at $t = 23.4$ μs ($\Delta a/\Delta t = 5060$ m/s), which are during the transition. In Fig. 18a a stress concentration ahead of and separated from that of the main crack is seen which reveals the formation of a daughter crack. In Fig. 18b, the mother and daughter crack begin to coalesce, while in Fig. 18c, the front of the daughter crack is propagating at 2470 m/s (faster than c_1^H), with the mother crack attached to the daughter crack. In Fig. 18d, there is only one crack moving at 5060 m/s with associated shear Mach waves. Subsequently, the sustained crack speed decreases to a value between $\sqrt{2}c_s^H$ and c_1^H. Note the change in scale in Fig. 18d; stress levels in the crack tip region are nearly a factor of two higher after the transition than before. A corresponding mother crack–daughter crack transition mechanism is also observed experimentally, as presented in Section 2, and the observed crack speed history in Fig. 8 is very similar to that in Fig. 17.

Contours of S_{22} (not presented here) show that S_{22} is compressive directly ahead of the crack at $t = 19.0$ μs and at $t = 21.0$ μs, and tensile during the transition when the crack speed exceeds c_1^H. After the transition, when the sustained crack speed is less than c_1^H, S_{22} ahead of the crack is again compressive. The same dependence of the sign of the near tip values of S_{22} on crack speed is seen for calculations with other values of impact velocity and pulse width in Fig. 16; when the crack speed is less than c_1^H, S_{22} is compressive directly ahead of the crack and tensile when the crack speed is greater than c_1^H. This is exactly opposite to what occurs in case 1 (Fig. 11) where $S_{22} < 0$ directly ahead of the crack when the crack speed is supersonic and $S_{22} > 0$ directly ahead of the crack tip when the crack speed is intersonic.

5. Discussion

The types of crack speed histories obtained computationally and experimentally are summarized in Fig. 19 which shows curves of crack speed, $\Delta a/\Delta t$, versus crack extension Δa. Fig. 19a shows the computed crack speeds for case 1, in which the composite is impacted on the notched side of the specimen (Fig. 2a). One experimental curve is shown in Fig. 19b. Curves 2 and 3 in Fig. 19a correspond to calculations for which pulse-like opening displacement jump and traction distributions along the bond line are predicted (Fig. 12). It remains to be seen whether or not these predictions are born

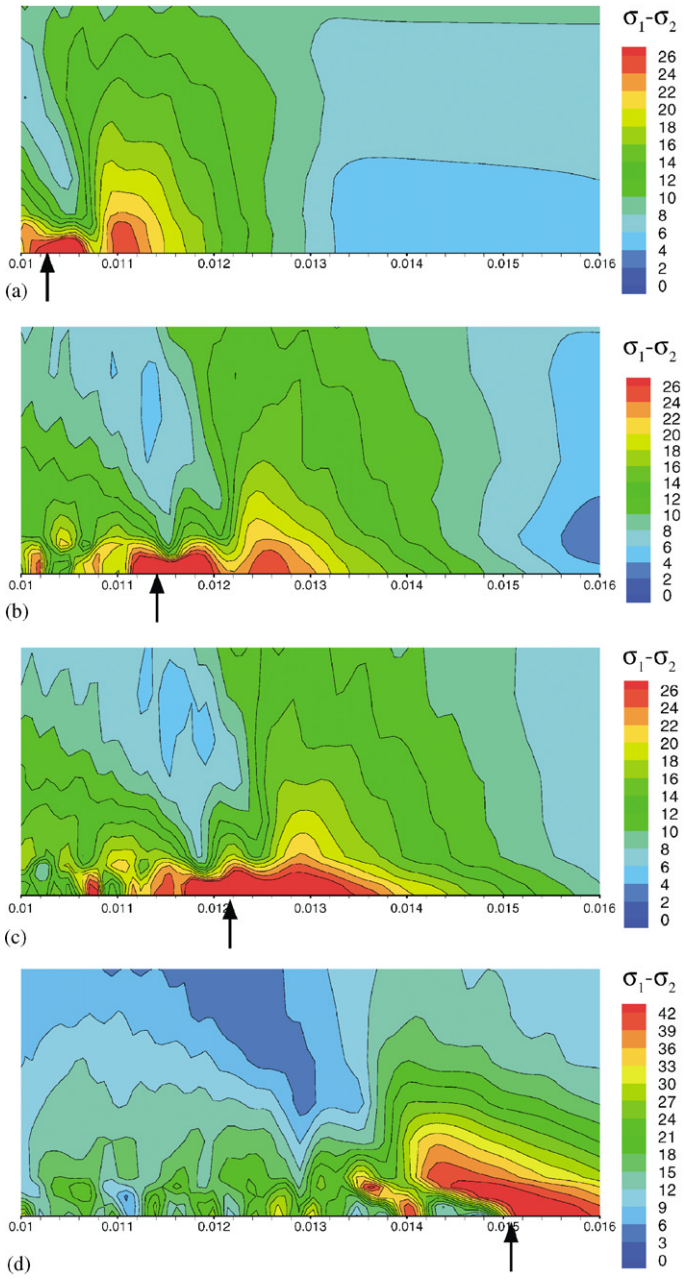

Fig. 18. Computed isochromatic fringe patterns (contours of $\sigma_1 - \sigma_2$) at 6 μs for case 3 with $V_1 = 20$ m/s and $t_p = 3$ μs, showing the emergence of a daughter crack and the coalescence with the mother crack. (a) $t = 19.0$ μs; $\Delta a/\Delta t = 1370$ m/s. (b) $t = 21.0$ μs; $\Delta a/\Delta t = 890$ m/s. (c) $t = 22.9$ μs; $\Delta a/\Delta t = 2470$ m/s. (d) $t = 23.4$ μs; $\Delta a/\Delta t = 5060$ m/s. The arrows show the current crack tip location and lengths marked on the axes are in m.

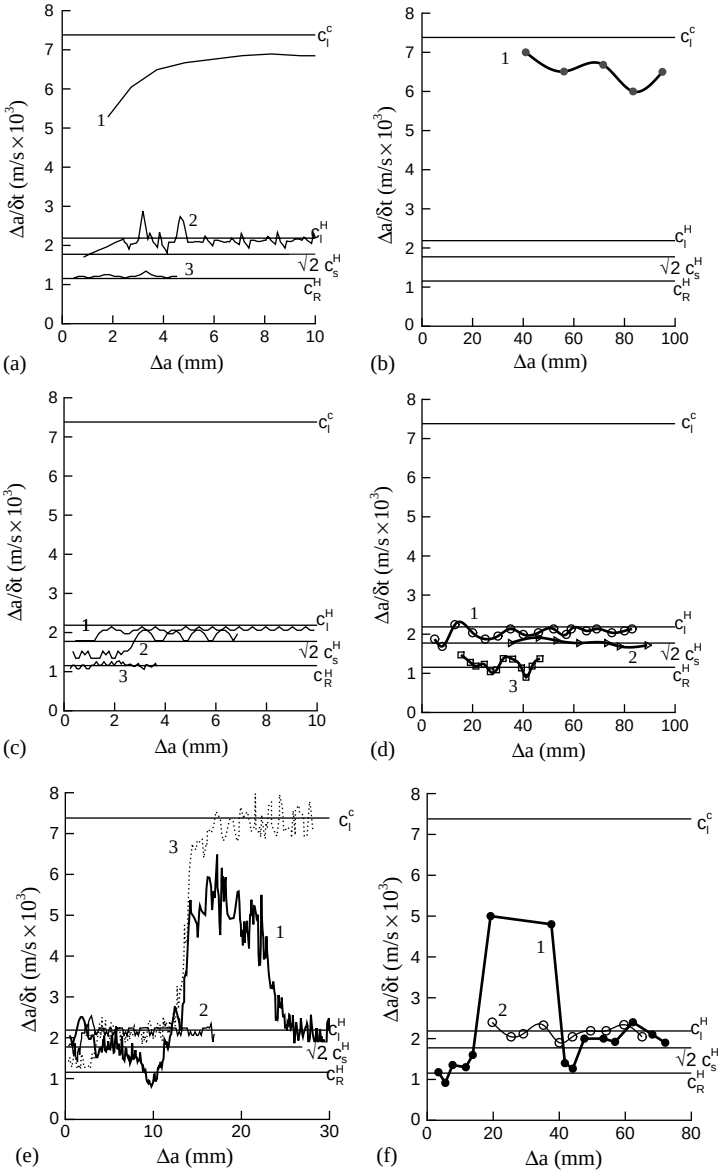

Fig. 19. Curves of crack speed, $\Delta a/\Delta t$ versus crack extension, Δa. (a) Numerical results for case 1 ($t_p = 25$ μs): curve 1 is for $V_1 = 20$ m/s; curve 2 is for $V_1 = 10$ m/s; curve 3 is for $V_1 = 5$ m/s. (b) Experimental results for case 1: curve 1 is for $V_1 = 35$ m/s. (c) Numerical results for case 2 ($t_p = 25$ μs): curve 1 is for $V_1 = 50$ m/s; curve 2 is for $V_1 = 8$ m/s; curve 3 is for $V_1 = 4$ m/s. (d) Experimental results for case 2: curve 1 is for $V_1 = 22$ m/s; curve 2 is for $V_1 = 40$ m/s; curve 3 is for $V_1 = 24$ m/s. (e) Numerical results for case 3: curve 1 is for $V_1 = 20$ m/s, $t_p = 3$ μs; curve 2 is for $V_1 = 15$ m/s, $t_p = 10$ μs; curve 3 is for $V_1 = 10$ m/s, $t_p = 25$ μs. (f) Experimental results for case 3: curve 1 is for $V_1 = 40$ m/s; curve 2 is for $V_1 = 27$ m/s;

out by experiment. The experimental and numerical crack speed versus crack extension curves for case 2, where the Homalite is impacted on the notched side of the specimen (Fig. 2b), are shown in Figs. 19c and d. In both the experiments and the computations, the sustained crack speeds do not exceed c_1^H for case 2. In Figs. 19e and f, the computed and experimental crack speed versus crack extension curves are compared for case 3, where impact occurs on the composite edge opposite the notch. In particular, the agreement for the crack speed history for curve 1, where the crack speed transitions from subsonic to intersonic via a mother–daughter crack mechanism, is excellent. For case 3, a sustained crack speed of c_1^c (curve 3 in Fig. 19e) was not obtained in the current set of experiments.

Computationally, sustained crack speeds of c_1^c are attained for both case 1 (Fig. 2a) and case 3 (Fig. 2c). The direction of relative sliding is opposite in these two cases; in case 1 the composite slides in the crack growth direction, whereas in case 3 the Homalite slides in the crack growth direction. When a sustained crack speed of c_1^c is attained in case 1, the normal tractions directly ahead of the crack tip are compressive, whereas at this speed in case 3 the normal tractions are tensile. Conversely, when the sustained crack speed is intersonic, i.e. between c_R^H and c_1^H, the normal tractions directly ahead of the crack tip are tensile in case 1 and compressive in case 3. In case 2, where the relative direction of sliding is the same as in case 3 and no sustained crack speeds greater than c_1^R are attained, the normal traction immediately ahead of the crack tip is compressive (as it is for case 3), but then oscillates (see Fig. 15). This suggests that, as for isotropic elastic-rigid bimaterial systems (Lambros and Rosakis, 1995; Liu et al., 1995) there is a crack speed at which the normal traction (and displacement jump) change sign, with the sense of the change depending on the sliding direction. However, for the bimaterial system considered here, that speed is not $\sqrt{2}c_s^H$.

Although there is excellent agreement between the experiments and the calculations regarding the crack speed regimes, the values for the crack initiation time and for the impact velocities required to reach the various regimes do not agree; crack initiation occurs later in the experiments than in the calculations and the impact velocity required to reach a given regime is larger. A significant difference between the experimental and computational configurations is that the experimental specimens are notched whereas a sharp crack is assumed in the computations so that the initiating stress concentration is greater in the calculations. Another possible factor contributing to the discrepancy is that the value used for the bond cohesive strength may not be representative of that in the experiments. Indeed, the experimental crack speed versus time curves in Figs. 6 and 8, where smaller values of the impact velocity give rise to higher sustained crack speeds, indicate that the bond strength is different for different specimens. Since one aim of this study was to test the predictive capability of the calculations, an estimate of the cohesive strength (half that of Homalite) was made and the values of characteristic length in Needleman and Rosakis (1999) were used so that there were no adjustable parameters. A current shortcoming of the cohesive surface framework is the difficulty in obtaining independent measurements of cohesive properties that can be used with confidence to make fracture predictions. The experiments and computations are however consistent in indicating that the sustained crack speed regimes depend primarily on the elastic properties of the two materials.

There is also very good agreement between the experimentally observed and the numerically calculated isochromatic fringe patterns in the Homalite. In particular, both the computed and experimental fringe patterns give a consistent picture of the mother–daughter crack mechanism that permits a subsonic crack to attain an intersonic crack speed (Figs. 7 and 18). For crack growth at supersonic speeds, the experimental and numerical fringe patterns exhibit a band of shear Mach waves first followed by a region with a vortical structure and then followed by a band of shear Mach waves focused at the supersonically moving crack tip (Figs. 3 and 10). Also seen in these figures are the complex stress concentration fringes along the bond line after the shear crack tip has passed. In the experiments, secondary cracks propagate from the bond line into the Homalite. The agreement between the computations, where crack growth is restricted to the bond line, and the experiments shows that this complex stress state is not a consequence of the secondary cracking, although the cracks may nucleate there because of the induced stress concentration. The agreement between the computed and experimental fringe patterns in Homalite gives confidence in the computed stress state in the composite which is not accessible experimentally.

The emergence of the pulse-like traction distribution in Fig. 12b is reminiscent of a behavior seen in dynamic rupture models introduced in seismology. In particular, the concept of a self-healing pulse, see e.g. Weertman (1980), Heaton (1990), Beeler and Tullis (1996), Andrews and Ben-Zion (1997), Zheng and Rice (1998), Cochard and Rice (2000), Adams (2001), Ranjith and Rice (2001) and Rice (2001), has been used to study shallow crustal earthquakes and involves the dynamic propagation, along a weak fault line, of frictional shear cracks of finite length whose moving trailing edge is followed by frictional locking. Opening pulse-like behavior at a frictional interface is associated with Schallamach waves, see e.g. Barquins (1985). The pulse-like normal traction distribution obtained in the present calculations, where the interfacial behavior is elastic, suggests the possibility that pulse-like behavior may be intimately related to the elastodynamics of interfacial separation (in certain regimes of crack speed) and may not require frictional dissipation to occur.

A main feature of the experimental and computational crack speed histories here, as in Needleman and Rosakis (1999) and Needleman (1999), is that crack propagation at a sustained speed only occurs in discrete crack speed regimes. Not all of the numerically predicted regimes were seen in the experiments. In the computations, the crack was forced to grow along the bond line; one possibility is that the tendency for the crack path to deviate from the bond line is so strong in some regimes that their experimental realization is effectively precluded, at least for the bimaterial system considered here. At least some of the crack speed regimes are separated by energetic barriers that require sufficient energy to be supplied to the crack tip region to be overcome, which can be supplied either through the loading wave or through a reflected wave catching up to the propagating crack. However, in the calculations at least, abrupt changes (from a crack speed below $\sqrt{2}c_s^H$ to one between $\sqrt{2}c_s^H$ and c_l^H) in crack speed occur for cases 2 and 3 that we could not correlate with a change in energy supplied to the crack tip region. In all cases, this change in sustained crack speed occurs after only a few millimeters of crack growth. One possibility is that the initial sustained crack speed is in an unstable regime and only after some crack growth does a fully developed

dynamic crack tip field emerge; then the crack speed shifts to a stable regime. This type of abrupt crack speed change was not seen in any of the calculations for case 1. It is perhaps worth noting that in cases 2 and 3 the direction of relative sliding is the same (i.e., the relative sliding of the Homalite is in the direction of crack growth).

6. Conclusions

We have investigated dynamic fracture along a fiber-reinforced epoxy composite–Homalite interface both experimentally and in numerical simulations. In the experiments, crack growth is observed using dynamic photoelasticity together with high-speed photography. The simulations are carried out using a cohesive surface formulation with both the material and cohesive constitutive relations taken to be elastic. In this formulation, crack growth, when it occurs, emerges as a natural outcome of the deformation history.

- Sustained crack growth occurs within discrete speed ranges delimited by characteristic elastic wave speeds; in particular, the Rayleigh wave speed of Homalite, c_R^H, the longitudinal wave speed of Homalite, c_l^H, and the longitudinal wave speed of the composite, c_l^c.
- The longitudinal wave speed of the composite, c_l^c appears to provide the upper limit to the sustainable crack speed.
- A pulse-like normal traction distribution was obtained along the bond line in the calculations, but remains to be observed experimentally.
- The experiments provide the first direct observations of: (i) the formation of a daughter crack facilitating the transition from a subsonic crack to an intersonic crack speed and (ii) interfacial crack speeds faster than any characteristic elastic wave speed of the more compliant material.
- There is excellent agreement between the numerically computed and experimentally observed attainable regimes of sustained crack speed and between the numerically computed and experimentally observed isochromatic fringe patterns (contours of maximum principal stress difference). Indeed, the occurrence of a sustained crack speed near c_l^c was predicted numerically and the calculations were used to design the experiments that captured this behavior.

Acknowledgements

Support from the Office of Naval Research through grants N00014-97-1-0179 and N00014-95-1-0453 is gratefully acknowledged.

References

Abraham, F.F., 2001. The atomic dynamics of fracture. J. Mech. Phys. Solids 49, 2095–2111.
Abraham, F.F., 2002. private communication.
Abraham, F.F., Gao, H., 2000. How fast can cracks propagate? Phys. Rev. Lett. 84, 3113–3116.

Achenbach, J.D., Epstein, H.I., 1967. Dynamic interaction of a layer and a half-space. J. Eng. Mech. 5, 27–42.

Adams, G.G., 2001. An intersonic slip pulse at a frictional interface between dissimilar materials. J. Appl. Mech. 68, 81–86.

Andrews, D.J., 1976. Rupture velocity of plane strain shear cracks. J. Geophys. Res. 81, 5679–5687.

Andrews, D.J., Ben-Zion, Y., 1997. Wrinkle-like slip pulse on a fault between different materials. J. Geophys. Res. 102, 553–571.

Barnett, D.M., Gavazza, S.D., Lothe, J., 1988. Slip waves along the interface between two anisotropic elastic half-spaces in sliding contact. Proc. R. Soc. London A 415, 389–419.

Barquins, M., 1985. Sliding friction of rubber and Schallamach waves—a review. Mater. Sci. Eng. 73, 45–63.

Beeler, N.M., Tullis, T.E., 1996. Self-healing slip pulses in dynamic rupture models due to velocity-dependent strength. Bull. Seismol. Soc. Am. 86, 1130–1148.

Belytschko, T., Chiapetta, R.L., Bartel, H.D., 1976. Efficient large scale non-linear transient analysis by finite elements. Int. J. Numer. Methods Eng. 10, 579–596.

Breitenfeld, M.S., Geubelle, P.H., 1997. Numerical analysis of dynamic debonding under 2d in-plane and 3d loading. Int. J. Fract. 85, 265–282.

Broberg, K.B., 1960. The propagation of a brittle crack. Arch. Fys. 18, 159–192.

Broberg, K.B., 1989. The near-tip field at high crack velocities. Int. J. Fract. 39, 1–13.

Brock, L.M., 2002. Interface crack extension at any constant speed in orthotropic or transversely isotropic bimaterials—I. general exact solutions. Int. J. Solids Struct. 39, 1165–1182.

Burridge, R., 1973. Admissible speeds for plane strain shear cracks with friction but lacking cohesion. Geo. J. Roy. Astron. Soc. 35, 439–455.

Cochard, A., Rice, J.R., 2000. Fault rupture between dissimilar materials: ill-posedness, regularization, and slip-pulse response. J. Geo. Res. 105, 25,891–25,907.

Coker, D., Rosakis, A.J., 2001. Experimental observations of intersonic crack growth in asymmetrically loaded, unidirectional composite plates. Phil. Mag. A 81, 571–595.

Dally, J.W., 1978. Dynamic photoelastic studies of stress wave propagation. In: Miklowitz, J., Achenbach, J.D. (Eds.), Modern Problems in Elastic Wave Propagation. Wiley, New York, pp. 3–21.

Dally, J.W., Riley, W.F., 1991. Experimental Stress Analysis. McGraw-Hill, New York.

Dwivedi, S.K., Espinosa, H.D., 2002. Modeling dynamic crack propagation in fiber reinforced composites including frictional effects. Mech. Mater., in press.

Freund, L.B., 1979. The mechanics of dynamic shear crack propagation. J. Geo. Res. 84, 2199–2209.

Freund, L.B., 1998. Dynamic Fracture Mechanics. Cambridge University Press, Cambridge.

Gao, H., Huang, Y., Gumbsch, P., Rosakis, A.J., 1999. On radiation-free transonic motion of cracks and dislocations. J. Mech. Phys. Solids 47, 1941–1961.

Geubelle, P.H., Kubair, D.V, 2001. Intersonic crack propagation in homogeneous media under shear-dominated loading: numerical analysis. J. Mech. Phys. Solids 49, 571–587.

Heaton, T.H., 1990. Evidence for and implications of self-healing pulses of slip in earthquake rupture. Phys. Earth. Planet. Inter. 64, 1–20.

Huang, Y., Wang, W., Liu, C., Rosakis, A.J., 1998. Intersonic crack growth in bimaterial interfaces: an investigation of crack face contact. J. Mech. Phys. Solids 46, 2233–2259.

Huang, Y., Wang, W., Liu, C., Rosakis, A.J., 1999. Intersonic crack growth in unidirectional fiber-reinforced composites. J. Mech. Phys. Solids 47, 1893–1916.

Hwang, C., Geubelle, P.H., 2000. A spectral scheme to simulate dynamic fracture problems in composites. CMES-Comp. Mod. Eng. Sci. 1, 4, 45–55.

Krieg, R.O., Key, S.W., 1973. Transient shell response by numerical time integration. Int. J. Numer. Methods Eng. 7, 273–286.

Lambros, J., Rosakis, A.J., 1995. Shear dominated transonic interfacial crack growth in a bimaterial—I: experimental observations. J. Mech. Phys. Solids 43, 169–188.

Liu, C., Lambros, J., Rosakis, A.J., 1993. Highly transient elasto-dynamic crack growth in a bimaterial interface: higher order asymptotic analysis and optical experiment. J. Mech. Phys. Solids 41, 1887–1954.

Liu, C., Huang, Y., Rosakis, A.J., 1995. Shear dominated transonic interfacial crack growth in a bimaterial—II: asymptotic fields and favorable velocity regimes. J. Mech. Phys. Solids 41, 1887–1954.

Lo, C.Y., Nakamura, T., Kushner, A., 1994. Computational analysis of dynamic crack propagation along bimaterial interfaces. Int. J. Solids Struct. 31, 145–168.

Needleman, A., 1987. A continuum model for void nucleation by inclusion debonding. J. Appl. Mech. 54, 525–531.

Needleman, A., 1999. An analysis of intersonic crack growth under shear loading. J. Appl. Mech. 66, 847–857.

Needleman, A., Rosakis, A.J., 1999. The effect of bond strength and loading rate on the conditions governing the attainment of intersonic crack growth along interfaces. J. Mech. Phys. Solids 47, 2411–2449.

Piva, A., Hasan, W., 1996. Effect of orthotropy on the intersonic shear crack propagation. J. Appl. Mech. 63, 933–938.

Ranjith, K., Rice, J.R., 2001. Slip dynamics at an interface between dissimilar materials. J. Mech. Phys. Solids 49, 341–361.

Ravi-Chandar, K., Knauss, W.G., 1984. An experimental investigation into dynamic fracture. 3. On steady-state crack propagation and crack branching. Int. J. Fract. 26, 141–154.

Rice, J.R., 2001. New perspectives on crack and fault dynamics. In: Aref, H., Philips, J.W. (Eds.), Mechanics for a New Millennium. Kluwer Academic Publishers, Dordrecht, pp. 1–24.

Rosakis, A.J., 2002. Intersonic shear cracks and fault ruptures. Adv. Phys. 51, 1189–1257.

Rosakis, A.J., Samudrala, O., Singh, R.P., Shukla, A., 1998. Intersonic crack propagating in bimaterial systems. J. Mech. Phys. Solids 46, 1789–1813.

Rosakis, A.J., Samudrala, O., Coker, D., 1999. Cracks faster than the shear wave speed. Science 284, 1337–1340.

Rosakis, A.J., Samudrala, O., Coker, D., 2000. Intersonic shear crack growth along weak planes. Mater. Res. Innov. 3, 236–243.

Samudrala, O., Huang, U.U., Rosakis, A.J., 2002. Subsonic and intersonic mode-II crack propagation with a rate-dependent cohesive zone. J. Mech. Phys. Solids 50, 1231–1268.

Sharon, E., Gross, S.P., Fineberg, J., 1996. Energy dissipation in dynamic fracture. Phys. Rev. Lett. 76, 2117–2120.

Sharon, E., Fineberg, J., 1999. Confirming the continuum theory of dynamic brittle fracture for fast cracks. Nature 397, 333–335.

Singh, R.P., Shukla, A., 1996. Subsonic and intersonic crack growth along a bimaterial interface. J. Appl. Mech. 63, 919–924.

Singh, R.P., Lambros, J., Shukla, A., Rosakis, A., 1997. Investigation of the mechanics of intersonic crack propagation along a bimaterial interface using coherent gradient sensing and photoelasticity. Proc. R. Soc. London A 453, 2649–2667.

Weertman, J., 1963. Dislocations moving uniformly on the interface between isotropic media of different elastic properties. J. Mech. Phys. Solids 11, 197–204.

Weertman, J., 1980. Unstable slippage across a fault that separates elastic media of different elastic constants. Geophys. J. Int. 85, 1455–1461.

Xu, X.-P., Needleman, A., 1993. Void nucleation by inclusion debonding in a crystal matrix. Modell. Simul. Mat. Sci. Engin. 1, 111–132.

Xu, X.-P., Needleman, A., 1994. Numerical simulations of fast crack growth in brittle solids. J. Mech. Phys. Solids 42, 1397–1434.

Xu, X.-P., Needleman, A., 1996. Numerical simulations of dynamic crack-growth along an interface. Int. J. Fract. 74, 289–324.

Xu, L.R., Rosakis, A.J., 2002. Impact failure characteristics in sandwich structures; part II: effects of impact speed and interfacial strength. Int. J. Solids Struct. 39, 4237–4248.

Yu, H., Yang, W., 1995. Mechanics of transonic debonding of a bimaterial interface: the in-plane case. J. Mech. Phys. Solids 43, 207–232.

Yu, C., Pandolfi, A., Ortiz, M., Coker, D., Rosakis, A.J., 2002. Three-dimensional modeling of intersonic crack growth in asymmetrically-loaded unidirectional composite plates. Int. J. Solids Struct., in press.

Zheng, G., Rice, J.R., 1998. Conditions under which velocity-weakening friction allows a self-healing versus a crack-like mode of rupture. Bull. Seismol. Soc. Am. 88, 1466–1483.